The Free Energy of NOAA Solar Active Region AR 11029

S.A. Gilchrist · M.S. Wheatland · K.D. Leka

Abstract
The NOAA active region AR 11029 was a small but highly active sunspot region which produced 73 *GOES* soft X-ray flares during its transit of the disk in late October 2009. The flares appear to show a departure from the well known power-law frequency-size distribution. Specifically, too few *GOES* C-class and no M-class flares were observed by comparison with a power-law distribution (Wheatland in *Astrophys. J.* **710**, 1324, 2010). This was conjectured to be due to the region having insufficient magnetic energy to power the missing large events. We construct nonlinear force-free extrapolations of the coronal magnetic field of active region AR 11029 using data taken on 24 October by the SOLIS Vector-SpectroMagnetograph (SOLIS/VSM), and data taken on 27 October by the *Hinode* Solar Optical Telescope SpectroPolarimeter (*Hinode*/SP). Force-free modeling with photospheric magnetogram data encounters problems because the magnetogram data are inconsistent with a force-free model. We employ a recently developed 'self-consistency' procedure which addresses this problem and accommodates uncertainties in the boundary data (Wheatland and Régnier in *Astrophys. J.* **700**, L88, 2009). We calculate the total energy and free energy of the self-consistent solution which provides a model for the coronal magnetic field of the active region. The free energy of the region is found to be $\approx 4 \times 10^{29}$ erg on 24 October, and $\approx 7 \times 10^{31}$ erg on 27 October. An order of magnitude scaling between RHESSI non-thermal energy and *GOES* peak X-ray flux is established from a sample of flares from the literature and is used to estimate flare energies from observed *GOES* peak X-ray flux. Based on the scaling, we conclude that the estimated free energy of AR 11029 on 27 October when the flaring rate peaked is sufficient to power M-class or X-class flares, and hence the modeling does not appear to support the hypothesis that the absence of large flares is due to the region having limited energy.

Keywords: Active Regions, Magnetic Fields, Corona

1. Introduction

The dynamics of the Sun's diffuse outer atmosphere, the corona, is dominated by the solar magnetic field (Aschwanden, 2004). Solar flares are the result of the explosive re-

S.A. Gilchrist · M.S. Wheatland
Sydney Institute for Astronomy, School of Physics, The University of
Sydney, NSW 2006, Australia
e-mail: s.gilchrist@physics.usyd.edu.au
K.D. Leka
NorthWest Research Associates, CoRA Division, 3380 Mitchell Lane,
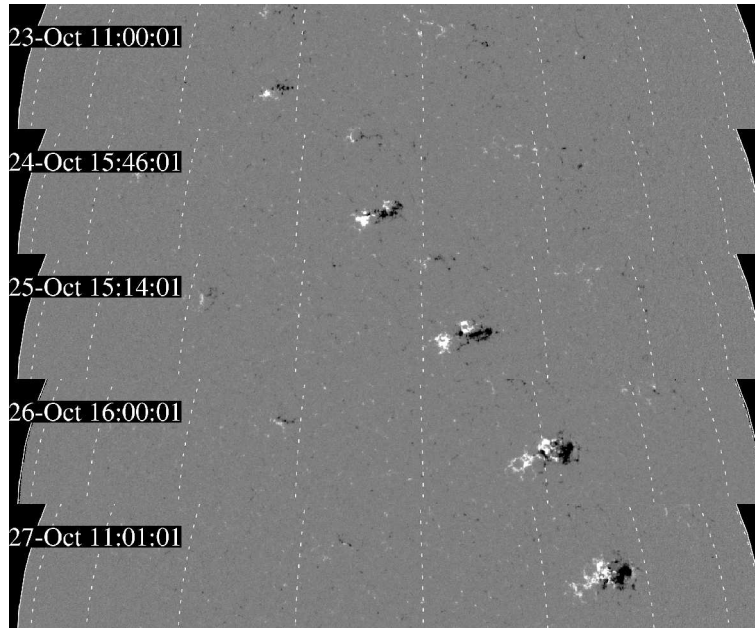Boulder, CO 80301, USA

Figure 1. Evolution of active region AR 11029 from 23 to 27 October 2009. The figure shows a collage of magnetograms from the Michelson Doppler Interferometer (MDI) aboard the *Solar and Heliospheric Observatory*. The data show the line-of-sight magnetic field $\approx 120\,\mathrm{km}$ above the base of the photosphere, and the field values saturate at $\pm 500\,\mathrm{gauss}\,(\mathrm{G})$. The times when the data are taken are indicated in the panels.

lease of magnetic energy from intense coronal magnetic fields associated with sunspots. Understanding the storage and release of magnetic energy in the corona is fundamental to understanding solar flares, and other coronal transient events (*e.g.* coronal mass ejections and transient X-ray brightenings).

The NOAA solar active region AR 11029 emerged on 21-22 October 2009, began flaring on 24 October 2009, and rotated off the disk on 1 November 2009. Figure 1 shows the evolution of the photospheric magnetic field of AR 11029 between 23 and 27 October as observed by the Michelson Doppler Interferometer (MDI) aboard the *Solar and Heliospheric Observatory*. Over the period shown the region grew in size and complexity. A detailed summary of the region's evolution during its transit of the disk is given by Wheatland (2010).

Active region AR 11029 was highly active, producing a large number of small flares during a period of pronounced solar minimum (Livingston and Penn, 2009). In total 73 soft X-ray events are listed in the event catalog[1] compiled from observations by the *Geostationary Operational Environmental Satellites* (*GOES*) during the region's transit of the disk. The majority are small *GOES* B-class events (peak 1-8 Å soft X-ray flux in the range $10^{-7}\mathrm{Wm}^{-2}$ to $10^{-6}\mathrm{Wm}^{-2}$). The largest is a *GOES* C2.2 event (peak soft X-ray flux of $2.2 \times 10^{-6}\mathrm{Wm}^{-2}$). No moderate sized M-class flares (peak flux $10^{-5}\,\mathrm{Wm}^{-2}$ to $10^{-4}\,\mathrm{Wm}^{-2}$) or large X-class flares (peak flux $\geq 10^{-4}\,\mathrm{Wm}^{-2}$) were produced.

The frequency and size of solar flares (by 'size' we mean a measure of the magnitude *e.g. GOES* peak flux) are related by a well known power-law distribution (*e.g.* Akabane 1956; Hudson 1991). This distribution is universal in the sense that the same power law index is observed at all times, for events occurring over the entire Sun and for events

---

[1]The *GOES* event catalog is found online at http://www.ngdc.noaa.gov.

that occur in different active regions (Wheatland, 2000). The power law in size reflects an underlying power law in the distribution of flare energies (Hudson, 1991).

Analysis of the statistics of the flares produced by active region AR 11029 using the *GOES* event data provides strong evidence for a departure from the expected power-law frequency-peak flux distribution for this region (Wheatland, 2010). The region produced fewer large events than expected given the number of small events, based on the power law distribution, and hence did not appear to follow the universal distribution.

The upper panel of Figure 2 shows the frequency-peak flux distribution for the flares produced by AR 11029 as a cumulative histogram (diamonds), and the curves show two model distributions. The straight line corresponds to a power-law model distribution $P(S) \sim S^{-\gamma}$ where S is the peak flux and γ is the power-law index. The curved line corresponds to a power law model with an exponential rollover at large event sizes $P(S) \sim S^{-\lambda} \exp(-S/\sigma)$ where λ is the power-law index for small S and σ is the rollover size. The vertical dotted line shows the peak flux above which the two models are assumed to apply ($10^{-7}\,\mathrm{Wm^{-2}}$). There is a noticeable departure from the power law at the large end of the scale. Given the data, a Bayesian model comparison taking into account all events showed that the rollover model was favored over the simple power-law model with an odds ratio[2] of ≈ 220 (Wheatland, 2010).

The absence of large flares was attributed by Wheatland (2010) to the region having insufficient energy to produce large events. In principle an upper bound on flare size must exist which reflects the finite energy stored in the active region's magnetic field (Hudson, 1991). However, it has proven difficult to observationally identify this effect in flare statistics (Hudson, 2007).

By determining the energy stored in the coronal magnetic field of active region AR 11029 it is in principle possible to test the hypothesis that the absence of large flares results from a lack of energy stored in the active region's magnetic field. The energy available for release in flares is called the free energy E_{f}, and is stored in the component of the coronal magnetic field generated by large scale electric currents in the corona (Priest and Forbes, 2002). Equivalently, the free energy is the energy in excess of the current free (potential) component *i.e.*

$$E_{\mathrm{f}} = E - E_0 = \frac{1}{2\mu_0} \int |\mathbf{B}|^2 dV - \frac{1}{2\mu_0} \int |\mathbf{B}_0|^2 dV, \tag{1}$$

where E is the total energy of the active region magnetic field $\mathbf{B}$, E_0 is the energy of the current free (potential) field $\mathbf{B}_0$, and the integrals are over the coronal volume of the active region. The potential field is uniquely defined in a finite volume by the normal component of the magnetic field on the closed surface surrounding this volume.

Determining the energy of an active region from Equation (1) requires knowledge of the magnetic field over the three dimensional coronal volume of the region. This information is difficult to obtain observationally. Solar magnetic fields affect the polarization of the Sun's optical emissions through the Zeeman effect (Landi Degl'Innocenti and Landolfi, 2004). This provides one diagnostic tool for inferring the solar magnetic field from spectropolarimetric measurements of magnetically sensitive lines, if such lines are available. Vector magnetograms are two-dimensional maps of the vector magnetic field

---

[2]The odds ratio is the relative probability that the data favors the rollover model over the power law model: a value of one indicates both models are equally likely, and a value of ≈ 220 indicates that the rollover model is ≈ 220 times more likely given the data (Jaynes, 2003).
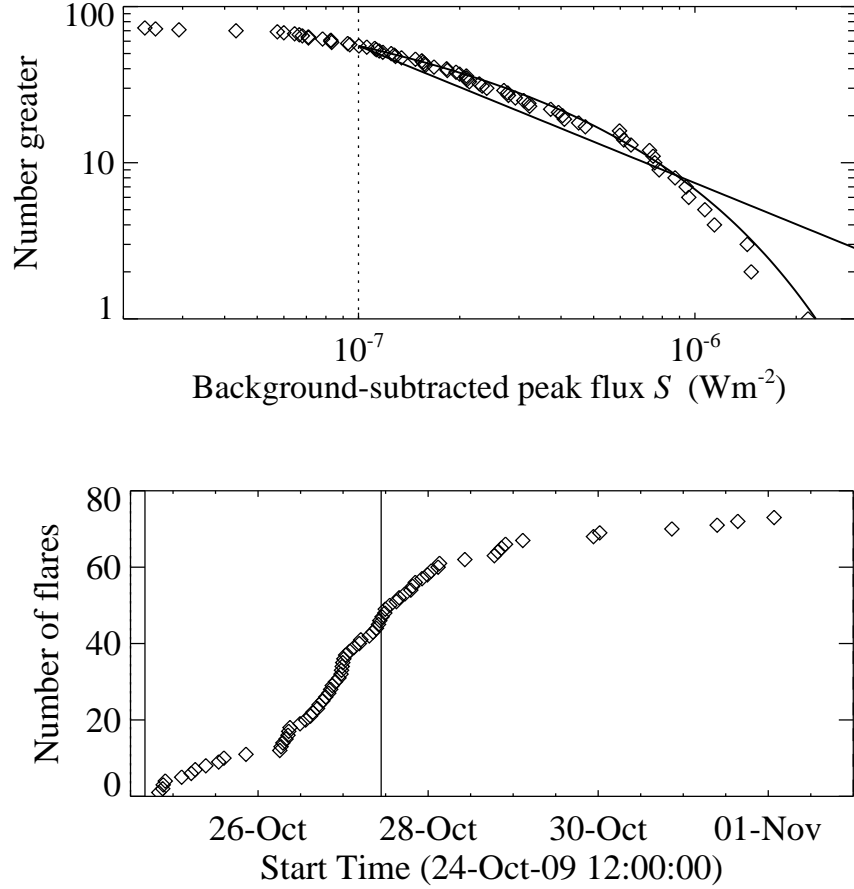
Figure 2. The upper panel shows the frequency-size distribution of soft X-ray flares for active region AR 11029 (Wheatland, 2010), plotted as a cumulative number distribution for the background subtracted peak soft X-ray flux of *GOES* events. The straight line shows a simple power law distribution, and the curved line shows a power law with an exponential rollover at large peak fluxes. The dotted vertical line shows the size threshold above which the models are assumed to apply ($10^{-7}\,\mathrm{Wm^{-2}}$). A Bayesian model comparison favors the rollover model to the straight power law with an odds ratio of ≈ 220 (Wheatland, 2010). The lower panel shows the cumulative number of *GOES* flares observed in active region AR 11029 versus time, between 24 October when the region began flaring, and 1 November when it rotated off the disk. The times when SOLIS/VSM and *Hinode*/SP magnetogram data are available are indicated in the lower panel by the solid vertical lines.

B close to the level of the photosphere, derived from spectropolarimetric measurements (Landi Degl'Innocenti and Landolfi, 2004). The field values are not coronal, but photospheric values. The coronal magnetic field cannot be determined observationally except in special cases (*e.g.* Hyder 1964), although a number of new methods based on radio (*e.g.* White and Kundu 1997; Lee *et al.* 1998) and infrared (*e.g.* Lin, Kuhn, and Coulter 2004) observations are under development.

The lack of observational methods for determining the coronal magnetic field motivates modeling of the coronal field from the photospheric vector magnetogram data [see reviews by Sakurai (1989) or more recently Wiegelmann (2008), for an overview of the so called 'reconstruction problem'], and such models permit estimates of the free energy of

the coronal magnetic field (*e.g.* Régnier and Priest 2007; Thalmann, Wiegelmann, and Raouafi 2008). The magnetic field on the lower boundary of the coronal volume is provided by the spectropolarimetric observations and this formally defines a boundary value problem for determining the coronal field, given a suitable model (Amari, Boulmezaoud, Aly, 2006). In this way the three dimensional coronal magnetic field can be 'extrapolated' from two dimensional magnetogram data.

Nonlinear force-free (NLFF) models of the coronal magnetic field assume the field is static and force free (*e.g.* Sturrock 1994). This means all non-magnetic forces are neglected and the magnetic Lorentz force is assumed to be self balancing, that is

$$\mathbf{J} \times \mathbf{B} = 0, \tag{2}$$

where $\mathbf{J}$ is the coronal electric current density. In practice a numerical approach is used to solve the force-free equations. A number of numerical methods have been developed (Wiegelmann, 2008) and tested on known solutions (Schrijver *et al.*, 2006). Section 2.1 provides further details of force-free modeling.

Force-free modeling encounters a number of problems in application to magnetogram data (De Rosa *et al.*, 2009). This appears to be primarily a result of the inconsistency between the force-free models and the boundary data. Whilst the corona may be close to force-free (Gary, 2001), the photosphere is subject to significant non-magnetic forces (Metcalf *et al.*, 1995; Gary, 2001). Metcalf *et al.* (1995) estimated that the solar atmosphere does not become force free until at least $400 \, \mathrm{km}$ above the base of the photosphere. Wheatland and Régnier (2009) developed a procedure based on an implementation of the Grad-Rubin method for calculating nonlinear force-free fields (Wheatland, 2007) which addresses the inconsistency between the data and the model. This approach identifies a force-free magnetic field solution with boundary conditions close to, but not exactly matching, the magnetogram boundary conditions. The resulting 'self-consistent' field may represent the coronal magnetic field. The self-consistency procedure can accommodate uncertainties in the boundary data (details of this method are given in Section 2.2). This method has previously been applied to vector magnetogram data without incorporating the uncertainties in the data (Wheatland and Régnier, 2009), and has recently been applied with uncertainties (Wheatland and Leka, 2011).

In this paper we use the Wheatland and Régnier (2009) self-consistency procedure to reconstruct the coronal magnetic field of AR 11029 from vector magnetogram data. The magnetograms are derived from spectropolarimetric data provided by the US National Solar Observatory's (NSO) Synoptic Optical Long term Investigations of the Sun Vector-SpectroMagnetograph (SOLIS/VSM), and the Solar Optical Telescope SpectroPolarimeter onboard the *Hinode* spacecraft (*Hinode*/SP). Based on the reconstructed coronal magnetic field we calculate the total energy stored in the active region and the free energy E_{f}, defined by Equation (1), and compare these results to a lower bound on the energy corresponding to the size of the largest observed *GOES* event produced by AR 11029.

This paper is structured as follows. Section 2 provides background on nonlinear force-free models and the self-consistency method, and Section 3 explains the use of the SOLIS/VSM and *Hinode*/SP data. Section 4 explains the application of the force-free model to the SOLIS/VSM and *Hinode*/SP data and presents the results of the modeling. Section 5 discusses the results, and Section 6 presents the conclusions. The Appendix contains a glossary of term used throughout the paper.

2. Background

2.1. Force-free Modeling of the Coronal Magnetic Field

The difficulties associated with observational determination of the coronal magnetic field have motivated numerical extrapolation methods which aim to 'reconstruct' the coronal magnetic field from photospheric spectropolarimetric data. This requires a model of the coronal magnetic field.

The nonlinear force-free model is a static model which assumes non-magnetic forces in the corona (*e.g.* gravity and pressure forces) are negligible compared to the magnetic (Lorentz) force. The latter assumption is approximately met when the plasma beta, defined as $\beta = 2\mu_0 p/|\mathbf{B}|^2$, where p is the gas pressure, is much less than unity. A force-free field may be defined as the solution[3] to the equations

$$\mathbf{B} \cdot \nabla \alpha = 0 \tag{3}$$

and

$$\nabla \times \mathbf{B} = \alpha \mathbf{B} \tag{4}$$

(Sturrock, 1994). Here $\mathbf{B}$ is the magnetic field vector and α is the force-free parameter, which is related to the electric current density $\mathbf{J} = \mu_0^{-1} \nabla \times \mathbf{B}$ by the relationship $\mathbf{J} = \alpha \mathbf{B}/\mu_0$.

Equations (3) and (4) are nonlinear in the general case (when α is a function of position, *i.e.* $\alpha = \alpha(\mathbf{r})$ where $\mathbf{r}$ is the position vector). The nonlinearity, and the mixed elliptic-hyperbolic character of the equations makes them difficult to solve, motivating a numerical approach. Several numerical methods for solving Equations (3) and (4) in a solar context have been developed [see reviews by Sakurai (1989) and Wiegelmann (2008)]. A version of the current-field iteration or Grad-Rubin approach, originally proposed by Grad and Rubin (1958), is used here (Wheatland, 2007).

The boundary conditions for solving the force-free equations are described by Bineau (1972) and Grad and Rubin (1958). In the solar context, the boundary conditions are B_n, the component of the magnetic field normal to the photosphere and α_0, the value of α on the photosphere over one polarity of the field *i.e.* over the region where $B_n > 0$, or the region where $B_n < 0$. We refer to the two choices, defined by the two different polarities, as the P and N choices respectively.

On the scale of an active region the curvature of the photosphere is often ignored (Gary and Hagyard, 1990), and Equations (3) and (4) are solved in the Cartesian half space $z \geq 0$, where $z = 0$ is the photosphere. In this case $B_n = B_z$, and the force-free parameter α on the photosphere is defined by

$$\alpha_0 = \frac{1}{B_z} \left(\frac{\partial B_y}{\partial x} - \frac{\partial B_x}{\partial y} \right) \bigg|_{z=0}. \tag{5}$$

The right hand side of Equation (5) may be estimated from photospheric vector magnetogram data, which we assume provides the vector components of $\mathbf{B}$ at $z = 0$.

---

[3]In this paper when we refer to a 'model' we mean the nonlinear force-free model defined by these equations. By 'solution' we mean a solution to these equations, for specific boundary conditions. The Appendix provides a glossary of terms.

The boundary value problem outlined in this section is for an infinite half space. To compute a numerical solution it is necessary to solve the equations on a finite grid of points. This introduces the problem that boundary conditions on $\mathbf{B}$ and α are unknown on the top and sides of the finite domain and force-free extrapolation codes must deal with this problem. The code used here assumes the magnetic field is periodic in the x and y directions, and that the force-free parameter α is zero on the top and side boundaries (Wheatland, 2007). Equation (3) requires that α is constant along field lines, and hence field lines which leave the top or side of the box have α set to zero along their length. This approach deals with the missing boundary data on α and ensures that $\nabla \cdot \mathbf{J} = 0$ is satisfied in the volume. The handling of missing boundary data is a source of uncertainty for the force-free modeling performed here, and in particular we expect the free energy to be decreased by the removal of currents implied by setting α to zero. In addition, images of the solution introduced by the periodicity will affect the solution. The effect of this should be small when the computational domain is large so the region of interest is isolated from the boundaries.

2.2. A Self-consistent Model of the Coronal Magnetic Field

Force-free modeling encounters problems when applied to photospheric magnetogram data (De Rosa *et al.*, 2009). Firstly, the iterative methods used to solve Equations (3) and (4) fail to strictly converge if large electric currents are present in the boundary data (De Rosa *et al.*, 2009). Secondly, methods using the formally correct boundary conditions given in Section 2.1 produce P and N solutions which differ both in terms of energy and field line connectivity. The second problem makes it difficult to estimate the energy of the region from the model because two solutions with different energy are obtained from the same magnetogram. These problems are in part due to noise in the data and uncertainties associated with the inversion of polarization measurements to give boundary magnetic field values, errors in the resolution of the 180-degree ambiguity in the direction of the field transverse to the line-of-sight (see Section 3.1), and errors introduced by the process of estimating photospheric values of α. However the fundamental problem is likely the inconsistency between the force-free model and the magnetogram data (Metcalf *et al.*, 1995).

The self-consistency procedure developed by Wheatland and Régnier (2009) addresses the inconsistency between the boundary data and the force-free model. The method iteratively modifies the values of α on the boundary, which we denote α_0, until the P and N solutions agree. The self-consistency procedure can also take into account the uncertainties on α_0 which we denote σ. We refer to repeat applications of the method involving modifications of α_0 as self-consistency 'cycles'.

Here we give a brief outline of the self-consistency procedure (see Wheatland and Régnier (2009) or Wheatland and Leka (2011) for a detailed explanation). A single self-consistency cycle can be broken into three steps. The first step involves constructing the P and N solutions from the the boundary data $B_z(x, y)$ and $\alpha_0(x, y)$. The Grad-Rubin method, an iterative method for solving Equations (3) and (4) (Grad and Rubin, 1958) is used, with an implementation in code described by Wheatland (2007). In general the P and N solutions obtained differ indicating the boundary data are inconsistent with a force-free model.

The second step of a self-consistency cycle involves constructing a second set of α values on the boundary, which we denote α_1, based on the connectivity of the P and N solutions. For a force-free field the parameter α is constant along field lines [an implication of Equation (3)]. Closed magnetic field lines connect points in the boundary

with $B_z > 0$ to points with $B_z < 0$, which defines a mapping between regions of P polarity and N polarity. The mapping defined by the field lines of the P solution maps values of α_0 in the P polarity to the N polarity (since α is constant along field lines). This defines a second set of α values over the N polarity. Similarly the N solution maps values of α_0 from the N polarity to the P polarity, which defines a second set of α values over the P polarity. Combined the values of α_0 mapped by the P and N solutions cover the entire lower boundary and we denote this second set of values α_1. In general $\alpha_0(x, y) \neq \alpha_1(x, y)$ unless the boundary data are consistent with a force-free model. Uncertainties on α_1, which we denote σ_1, are constructed from σ in the same way that α_1 is constructed from α_0.

The third step involves constructing a new set of α values on the lower boundary based on α_0 and α_1. The self-consistency procedure treats α_0 and α_1 as two separate observations of α on the lower boundary and Bayesian probability is used to decide on the most probable value at each boundary point given the uncertainties σ and σ_1 (Jaynes, 2003). Assuming the uncertainties σ (and by construction also σ_1) are Gaussian uncertainties, the new distribution of α on the lower boundary is

$$\alpha_{\text{new}} = \frac{\alpha_0/\sigma^2 + \alpha_1/\sigma_1^2}{1/\sigma^2 + 1/\sigma_1^2}. \tag{6}$$

If all uncertainties are equal then α_{new} is the average of the two values at each point *i.e.* $\alpha_{\text{new}} = (\alpha_0 + \alpha_1)/2$. An important property of Equation (6) is that α_{new} is unchanged under a global rescaling of the uncertainties σ and σ_1, *i.e.* Equation (6) is unchanged by the replacement $\sigma \to C\sigma$, where C is a constant. Hence the absolute value of σ at a point is not important: only the value with respect to other points is important.

The process of constructing P and N solutions and then applying Equation (6) (all three steps) is called a 'self-consistency cycle'. This procedure is iterated until $\alpha_0 = \alpha_1$ at all points in the boundary: a single force-free solution (a 'self-consistent' solution) is obtained. In Wheatland and Régnier (2009) the self-consistency procedure was demonstrated in application to data from AR 10953, with uncertainties assumed equal at all boundary points, and in Wheatland and Leka (2011) the calculation was repeated with uncertainties derived from the spectropolarimetric inversion. This paper follows the approach of Wheatland and Leka (2011).

3. Data and Modeling

Vector magnetogram data for active region AR 11029 are available from the ground based SOLIS Vector-SpectroMagnetograph (SOLIS/VSM), and from the Solar Optical Telescope SpectroPolarimeter on board the *Hinode* satellite (*Hinode*/SP). One SOLIS/VSM magnetogram per day is available for 24, 25, 26 and 28 October, and one *Hinode*/SP magnetogram per day is available from 24-29 October. All magnetograms are derived from observations of the Fe I (630nm) multiplet which provides the vector magnetic field close to the level of the photosphere ($\approx 250\,\text{km}$ above the base of the photosphere).

From the available data we use only the SOLIS/VSM magnetogram for 24 October and the *Hinode*/SP magnetogram for 27 October to derive the relevant boundary conditions for force-free modeling, as outlined in Section 2.1. We exclude the data for 28 and 29 October because the active region was too close to the limb, where projections effects become prohibitive. We exclude the *Hinode*/SP data for 24-26 October because for these days most of the active region lies outside the *Hinode*/SP field of view. We

exclude the SOLIS/VSM data for 25 and 26 October because the magnetograms appear to contain significant systematic errors and are not suitable for force-free modeling. In particular the component of the magnetic field transverse to the line of sight shows a strongly preferred direction which we attribute to the result of systematic error.

The lower panel of Figure 2 shows the times of the acceptable magnetogram observations (solid vertical lines) compared with the flare history of the region. The magnetogram data requires ≈ 10 minutes of integration time in the case of SOLIS/VSM and ≈ 60 minutes of integration time in the case of *Hinode*/SP. The region first began flaring on 24 October producing several small *GOES* A-class and B-class, and the SOLIS/VSM magnetogram data are taken on this day. The flaring rate for the region peaked on 26 and 27 October and the *Hinode*/SP magnetogram data are obtained during this interval.

3.1. SOLIS/VSM Data

The National Solar Observatory SOLIS/VSM provides Milne-Eddington inverted vector magnetograms, and 'Quicklook' data consisting of initial estimates of the vector magnetic field produced prior to Milne-Eddington inversion (Henney, Keller, and Harvey, 2006). Both full disk magnetograms and cropped data centered on individual active regions are available online[4]. The online data provide the magnetic field vector close to the photosphere in terms of a line-of-sight component and a component transverse to the line of sight (Henney, Keller, and Harvey, 2006). The transverse component is further decomposed into a magnitude and direction defined by the azimuthal angle. The inversion is performed by the NSO and details are given in Henney, Keller, and Harvey (2006).

The magnetogram for 24 October is obtained at $16\!:\!05$ (UT) and is 236×236 pixels in size with a spatial resolution of $1.1''$ per pixel. The magnetogram covers an area of $267'' \times 267''$ corresponding to 195×196 Mm on the photosphere. The NSO also provides Quicklook data for the same day. Over regions of the photosphere where the magnetic field is weak there are gaps in the Milne-Eddington data where inversion in not performed due to a poor signal to noise ratio. We embed Quicklook data directly into the Milne-Eddington data to fill these gaps, following the advice provided by the NSO[5].

As explained in Section 2.1 force-free modeling is performed in a locally flat Cartesian coordinate system defined on the photosphere, and we refer to this coordinate system as helioplanar coordinates. The magnetogram is provided on a uniform grid on a plane perpendicular to the line of sight. We map the magnetogram to a helioplanar system using the transformations given in Venkatakrishnan, Hagyard, and Hathaway (1988). The helioplanar coordinate system is defined on a plane tangent to the solar surface at a point at the center of the active region. The axes of this system are oriented such that the x and y axes align with solar west and north respectively, and the z axis is normal to the photosphere. Owing to projection effects after mapping, the grid on which the magnetic field is defined is no longer regularly spaced. We regrid the magnetogram onto a larger (in number of grid points) uniform grid with the same spatial resolution ($1.1''$ per pixel) as the original data. Since the active region is close to disk center on 24 October the projection effects are small.

---

[4]See http://solis.nso.edu.

[5]See the introduction to SOLIS/VSM data at http://solis.nso.edu/vsm/vsm_image_info3.html.

The spectropolarimetrically derived azimuthal angle contains an inherent 180° ambiguity (Landi Degl'Innocenti and Landolfi, 2004) which must be resolved to determine the magnetic field components (B_x, B_y and B_z) needed to derive boundary conditions for force-free modeling. Several procedures exist for resolving the 180° ambiguity [see Metcalf *et al.* (2006) and references therein], and here we use the 'minimum energy' method developed by Metcalf (1994). This method determines the azimuthal angle by requiring the ambiguity-resolved field to simultaneously minimize $|\nabla \cdot \mathbf{B}|$ and $|\mathbf{J}|^2$ over the magnetogram. The optimal magnetic field configuration is found using the general optimization procedure of simulated annealing (Press *et al.*, 1992). We note that the NSO/SOLIS provides ambiguity-resolved data using a different resolution method (Georgoulis, 2005), but we have chosen to perform this step again using the minimum energy procedure.

The boundary conditions for force-free modeling are the component of the magnetic field normal to the photosphere, which corresponds to the B_z values in the regridded magnetogram, and the force-free parameter α on the photosphere derived from the values of B_x and B_y in the magnetogram using Equation (5). The partial derivatives in Equation (5) are approximated using centered differencing (Press *et al.*, 1992). The boundary values on α are set to zero at points where $|B_z| < 0.01 \times \max(|B_z|)$ because the ratio J_z/B_z is inaccurate in regions where B_z is small.

The final boundary conditions after projection and regridding are shown in Figures 3 and 4. Figure 3 shows the boundary conditions for B_z (upper panel), and the boundary conditions for J_z (lower panel). Figure 4 shows the force-free parameter α_0, and the signal to noise ratio $|\alpha_0|/\sigma$ for α_0 where σ represents the approximate uncertainty in the α_0 value estimated using the B_z boundary value, as explained in Section 3.4. In both Figures 3 and 4, the data saturate at a particular threshold value which is below the maximum in the data, by which we mean all points above the threshold appear with the same color. This is done to provide a good contrast between large and small data values, and to diminish the appearance of outliers. For the panels showing J_z and α_0 only points where the signal to noise ratio $|\alpha_0|/\sigma$ is three standard deviations above the mean signal to noise ratio are represented, points where $|\alpha_0|/\sigma = 0$ are excluded when computing the mean and standard deviation. This criteria is chosen because it is independent of the magnitude of σ which is arbitrary for the SOLIS/VSM data (see Section 3.4). Only the central portion of the data is shown in the two panels because the boundary data values (B_z, J_z and α_0) outside the central region are comparatively small and are not visible with the chosen scale.

3.2. *Hinode*/SP Magnetogram Data

The *Hinode*/SP vector magnetogram data for 27 October is derived from spectropolarimetric data from the Solar Optical Telescope/SpectroPolarimeter aboard the *Hinode* satellite (Kosugi *et al.*, 2007; Tsuneta *et al.*, 2008). The 'fast-scan' map obtained at 10:45 (UT) is spatially sampled at $0.32''$, and covers a relatively small $360'' \times 164''$ field of view. The data are inverted using the High Altitude Observatory (HAO) Milne-Eddington inversion code (Skumanich and Lites, 1987; Lites and Skumanich, 1990; Lites *et al.*, 1993), which has been modified for *Hinode*/SP data (revised code courtesy B. Lites, HAO/NCAR). Ambiguity resolution is performed using an implementation[6] of the minimum energy procedure (Leka, Barnes, and Crouch, 2009).

For the *Hinode*/SP data for 27 October uncertainties in the three components of the magnetic field ($\sigma_x, \sigma_y, \sigma_z$) are derived during the Milne-Eddington inversion. These are

---

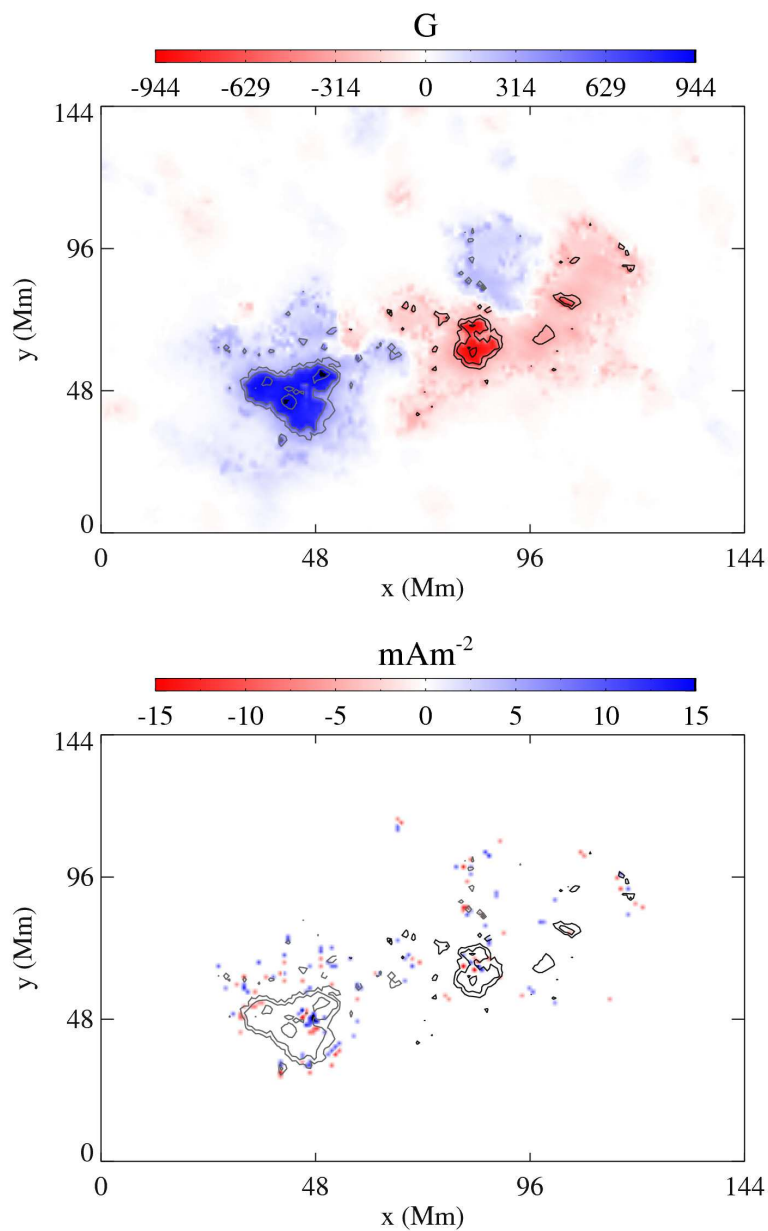[6]Available at http://www.cora.nwra.com/AMBIG/.

Figure 3. The central part of part of the SOLIS/VSM vector magnetogram data for 24 October. The upper panel shows B_z and the lower panel shows J_z. The data are colored blue when positive, white when zero, and red when negative. Contours of B_z are superimposed on the data, with contours separated by intervals of 300 G. The contours are black where $B_z < 0$ and light gray where $B_z > 0$. The values of B_z (upper panel) have been saturated at $\pm 944\,\mathrm{G}$ with a maximum value of 961 G. The values of J_z (lower panel) have been saturated at $\pm 15\,\mathrm{mAm}^{-2}$ with a maximum value of 23 mAm^{-2}. In the lower panel only points where $|\alpha_0|/\sigma$ is three standard deviations above the mean are shown.
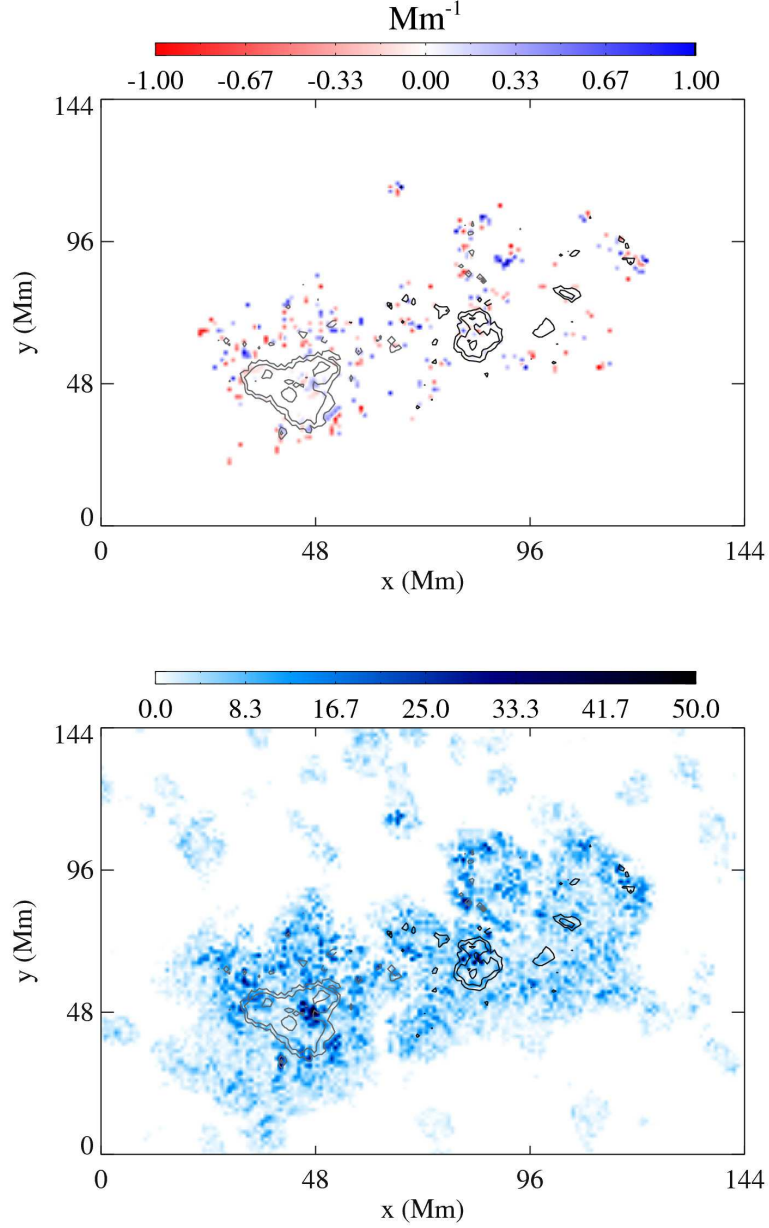
Figure 4. Boundary conditions on the force-free parameter obtained from the SOLIS/VSM vector magnetogram data for 24 October. The upper panel shows α_0 and the lower panel shows the signal to noise ratio $|\alpha_0|/\sigma$. The data are colored blue when positive, white when zero, and red when negative. Contours of B_z are superimposed on the data, with the contours separated by $300\,\mathrm{G}$. The contours are black where $B_z < 0$ and light gray where $B_z > 0$. The values of α_0 (upper panel) have been saturated at $\pm 1\,\mathrm{Mm}^{-1}$ with a maximum value of $3.7\,\mathrm{Mm}^{-1}$. The values of $|\alpha_0|/\sigma$ (lower panel) have been saturated at 50 with a maximum value of 67. In the upper panel only points where $|\alpha_0|/\sigma$ is three standard deviations above the mean are shown.

based on the uncertainty in the χ^2 fit of the synthetic Stokes profiles to the observed Stokes profiles. The uncertainties are then propagated through the projection, regridding and ambiguity resolution to derive uncertainties for α_0. These uncertainties are a measure of how well the artificial Milne-Eddington profiles fit the observed profiles. They do not take into account the approximation of the Milne-Eddington atmosphere or systematic errors in the observations of the Stokes profiles. Therefore they may be considered lower bounds to the real uncertainties. Some parameter-dependence is introduced into the method of simulated annealing by the choice of a 'cooling schedule' (Press *et al.*, 1992). We note that some data points are particularly sensitive to the choice of schedule, but overall the large scale structure of the ambiguity-resolved magnetogram appears independent of the choice. Large uncertainties are assigned to points which depend strongly on the choice of cooling schedule to reflect this parameter dependence.

The resulting vector magnetic components and uncertainties from the *Hinode*/SP data are re-mapped to a helioplanar $1''$ grid. The *Hinode*/SP field of view is small and only covers the main portion of the active region. As explained in Section 2.1 when performing force-free modeling it is important to isolate the region of interest from the boundaries to limit the influence of the boundaries on the solution. As with other studies involving *Hinode*/SP data (*e.g.* Wheatland and Leka 2011; De Rosa *et al.* 2009) the field of view is expanded by adding line-of-sight data from the Michelson Doppler Imager on the *Solar and Heliospheric Observatory* (Scherrer *et al.*, 1995) around the *Hinode*/SP data. A map of B_z is constructed using a potential field matching the observed line-of-sight magnetic field values in the boundary, and this is also remapped onto a $1''$ grid. After coalignment between the two data sources, an apodizing function is applied at the boundaries of the two data sets to ensure a smooth transition between data values. This procedure follows Wheatland and Leka (2011), and improves upon a method used in De Rosa *et al.* (2009). The final size of the boundary data is 440×300 pixels, covering a region on the photosphere of size 320×220 Mm.

The data are shown in Figures 5 and 6. The vertical magnetic field B_z (upper panel) and vertical current density J_z (lower panel) are shown in Figure 5. The presentation of the data follows the format used in Figures 3 and 4. Approximate uncertainties σ in the α_0 values are provided by the spectropolarimetric inversion, for the *Hinode*/SP data points. Figure 6 shows the force-free parameter α_0 (upper panel) and the signal-to-noise ratio $|\alpha_0|/\sigma$ (lower panel). For the panels showing J_z and α_0 only points where the signal to noise ratio $|\alpha_0|/\sigma$ is three standard deviations above the mean signal to noise ratio are represented, points where $|\alpha_0|/\sigma = 0$ are excluded when computing the mean and standard deviation. Only the central portion of the data is shown in the two panels because the boundary data values (B_z, J_z and α_0) outside the central region are comparatively small and are not visible with the chosen scale.

3.3. Flux Balance

The integral of B_z over the magnetogram defines the net magnetic flux across the observed region of the photosphere. If the net flux is zero then the magnetogram is said to be flux balanced. Flux balance is not essential for the force-free modeling procedure used here, but if the flux is unbalanced a greater number of field lines leave the top and sides of the computational domain in order to satisfy $\nabla \cdot \mathbf{B} = 0$ globally. As discussed in Section 2.1 boundary conditions are not known on the top and side boundaries of the domain and the force-free code sets $\alpha = 0$ along field lines which leave the domain via these boundaries (Wheatland, 2007). The currents and therefore the free energy tend
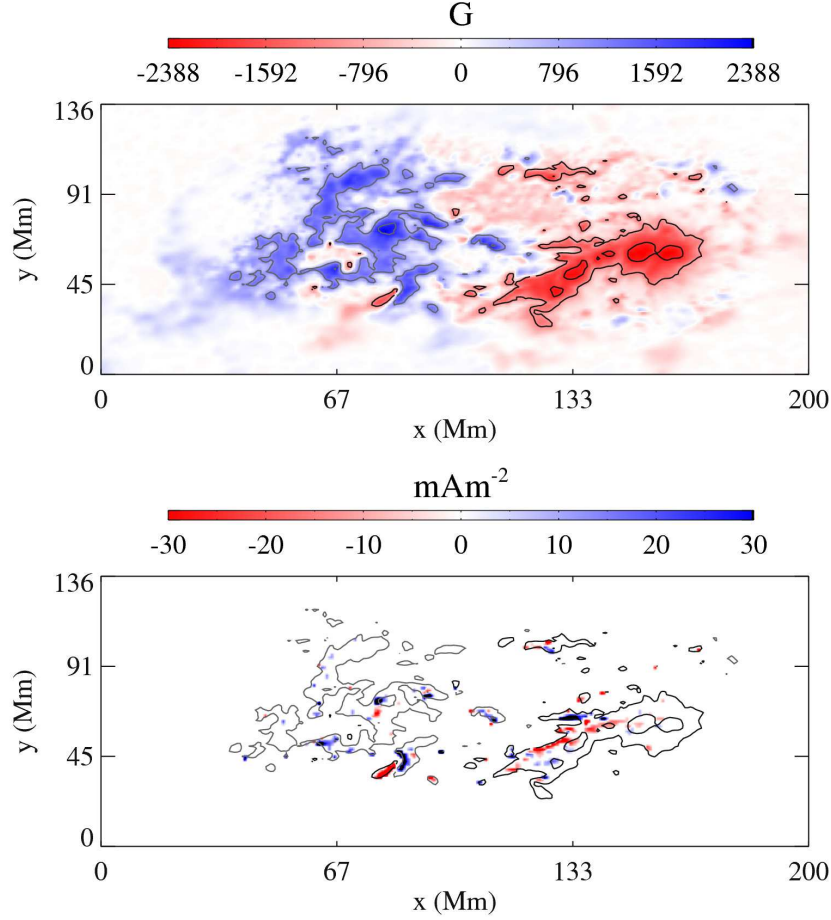
Figure 5. The central part of the *Hinode*/SP vector magnetogram data for 27 October. The upper panel shows B_z and the lower panel shows J_z. The data are colored blue when positive, white when zero, and red when negative. Contours of B_z are superimposed on the data, with contours separated by intervals of 1000 G. The contours are black where $B_z < 0$ and light gray where $B_z > 0$. The values of B_z (upper panel) have been saturated at ± 2448 G with a maximum value of 2388 G. The values of J_z (lower panel) have been saturated at ± 30 mAm^{-2} with a maximum value of 144 mAm^{-2}. In the lower panel only points where $|\alpha_0|/\sigma$ is three standard deviations above the mean are shown.

to be reduced by this procedure. The effect of the boundaries on the energy estimates is likely to be less pronounced if the magnetogram is flux balanced.

A practical measure of flux balance is the relative flux balance, defined as

$$\Phi_B = \frac{\int B_z dA}{\int |B_z| dA} \tag{7}$$

where the integrals are over the magnetogram area. The integrals in Equation (7) are evaluated numerically using the two-dimensional trapezoidal rule. The results are listed in the right-hand column in Table 1.

We consider a Φ_B of less than 1% acceptable. The *Hinode*/SP magnetogram for 27 October meets this requirement, but the SOLIS/VSM magnetogram for 24 October does not. To flux balance the SOLIS/VSM data a buffer region of constant B_z is
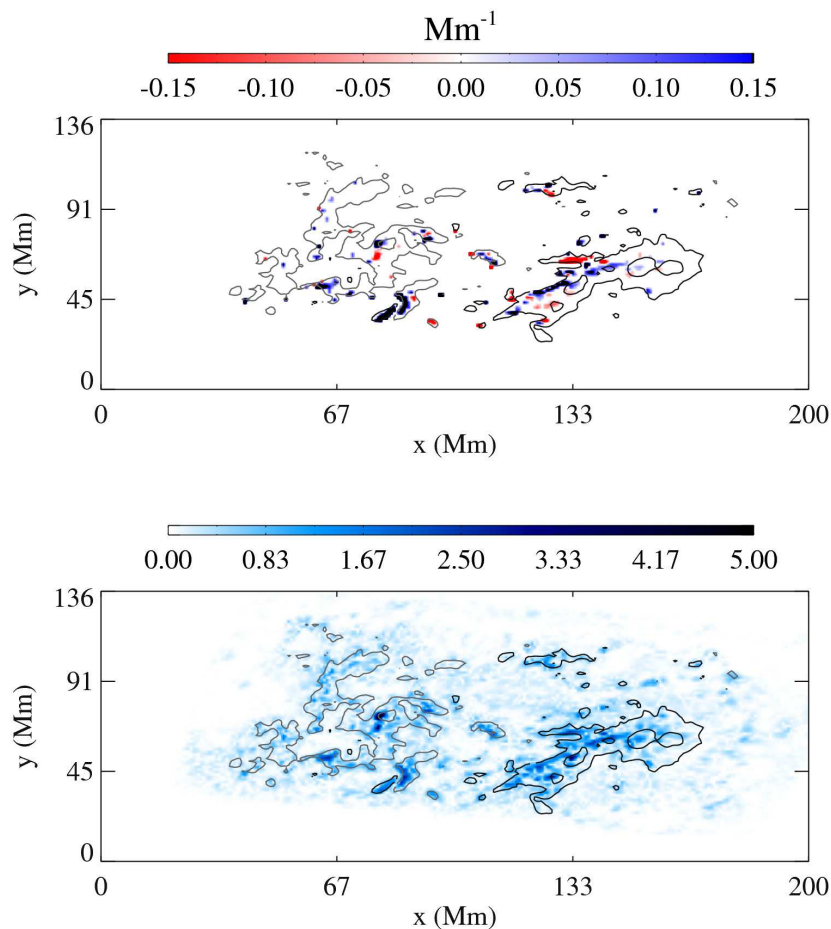
Figure 6. Boundary conditions on the force-free parameter obtained from the *Hinode*/SP vector magnetogram data for 27 October. The upper panel shows α_0 and the lower panel shows the signal to noise ratio $|\alpha_0|/\sigma$. The data are colored blue when positive, white when zero, and red when negative. Contours of B_z are superimposed on the data, with the contours separated by 1000 G. The contours are black where $B_z < 0$ and light gray where $B_z > 0$. The values of α_0 (upper panel) have been saturated at $\pm 0.15\,\mathrm{Mm}^{-1}$ with a maximum value of $1.9\,\mathrm{Mm}^{-1}$. The values of $|\alpha_0|/\sigma$ (lower panel) have been saturated at five with a maximum value of 5.4. In the upper panel only points where $|\alpha_0|/\sigma$ is three standard deviations above the mean are shown.

added around the border of the magnetogram. The magnitude of the field in the buffer region satisfies $|B_z| < 0.01 \times \max(|B_z|)$, and hence the buffer region is considered weak field by our previous definition (see Section 3.1). In the buffer the magnitude of B_z is $9.3\,\mathrm{gauss}\,(\mathrm{G})$ (the weak field threshold is $9.6\,\mathrm{G}$), and the value of α_0 is set to zero everywhere in the buffer. The total size of the magnetogram with the buffer added is 270×270 grid points, and the resolution of the data remains the same ($1.1''$ per pixel). The final size of the region including the flux buffer is $222 \times 222\,\mathrm{Mm}$.

3.4. Phenomenological Uncertainties for SOLIS/VSM Data

Uncertainties are provided with the *Hinode*/SP data based on spectropolarimetric inversion of the data (as explained in Section 3.2), but are not available for the SOLIS/VSM data for 24 October. Instead we make a simple estimate for the uncertainties

based on the magnitude of B_z at each boundary point. Specifically we introduce a phenomenological uncertainty defined by

$$L_x \sigma(x, y) = \begin{cases} 0.01 & \text{for the flux buffer region;} \\ B_{\mathrm{m}}/|B_z(x, y)| & \text{where } |B_z/B_{\mathrm{m}}| > 0.01 \\ 100 & \text{where } |B_z/B_{\mathrm{m}}| < 0.01 \end{cases} \tag{8}$$

Equation (8) is written in non-dimensional units. The magnetic field is scaled by $B_{\mathrm{m}} = \max(|B_z|)$, the maximum value of $|B_z|$, and σ is scaled by L_x, the transverse length of the magnetogram. Points in the flux buffer are assigned a small constant uncertainty, which ensures $\alpha_0 = 0$ for this region during the self-consistency procedure. A relatively large uncertainty ($L_x \sigma = 100$, in non-dimensional units) is assigned to points in weak field regions where α_0 has been set to zero (see Section 3.1).

The phenomenological scaling $\sigma(x, y) \sim 1/|B_z(x, y)|$ for the SOLIS/VSM data region is based on inspection of the inversion-based uncertainties for the *Hinode*/SP data for 27 October.

Figure 7 shows $P(\sigma, |B_z|)^{1/4}$, where $P(\sigma, |B_z|)$ is the distribution of the inversion-based uncertainties for the *Hinode*/SP data for 27 October over field strength and uncertainty in α_0 *i.e.* the fraction of points with field value $|B_z|$ and uncertainty σ. We have applied a nonlinear scaling to the distribution so that strong field regions with small values of $P(\sigma, |B_z|)$ are visible. The solid line shows $\sigma = 100\,\mathrm{Mm}^{-1}/|B_z|$ with B_z in gauss, to illustrate $\sigma \sim 1/|B_z|$ dependence for comparison. The choice of the factor $100\,\mathrm{Mm}^{-1}$ is arbitrary. The figure shows that the simple phenomenological scaling implied by Equation (8) is accurate for a majority of data points, although their is notable departure for large values of $|B_z|$.

It should be noted that, according to Equation (6), the exact magnitude of the uncertainties is not important for the self-consistency averaging procedure [see discussion following Equation (6)]. Only the relative size of uncertainties at different points is important.

Although, due to the departure from the $\sigma \sim 1/|B_z|$ scaling for large values of $|B_z|$ we expect that the uncertainties in strong field regions are underestimated relative to weak field regions.

3.5. Force-free Modeling Using SOLIS/VSM and *Hinode*/SP Data

Force-free solutions are calculated using the code of Wheatland (2007) and the self-consistency procedure of Wheatland and Régnier (2009). The boundary conditions derived from the SOLIS/VSM and *Hinode*/SP vector magnetogram data described in Sections 3.1 and 3.2 are used. The initial magnetic field for the Grad-Rubin iteration is a potential field calculated using a Fourier solution to Poisson's equation. The computational domain used is a uniform three dimensional Cartesian grid with transverse dimensions (*i.e.* the x and y dimensions) matching the dimensions of the magnetogram which forms the lower boundary at $z = 0$. The vertical dimension (*i.e.* z) is 128 points high for the SOLIS/VSM data and 200 points high for the *Hinode*/SP data. The resulting dimensions of the grids are $270 \times 270 \times 128$ points for 24 October, and $440 \times 300 \times 200$ points for 27 October. The grid spacing is uniform in each direction. We summarize the size, maximum magnetic field, and flux balance of the data in Table 1.
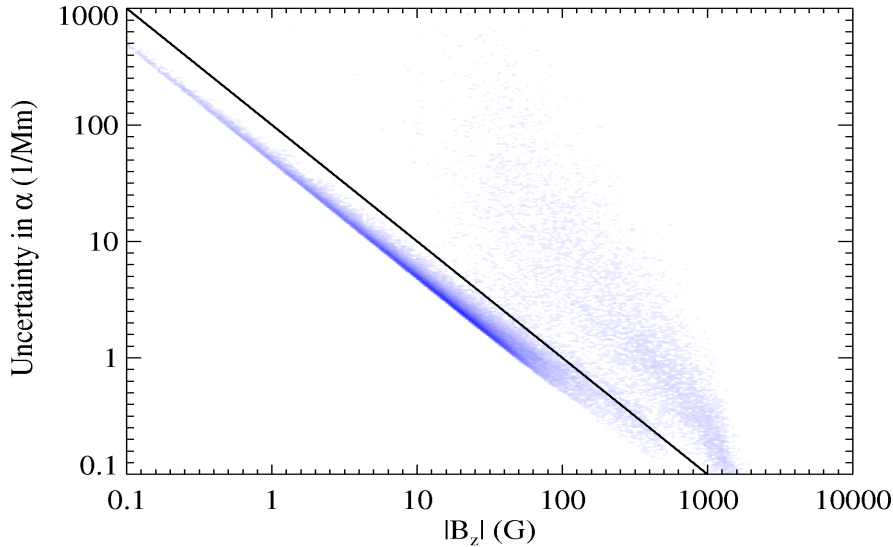
Figure 7. The relationship between the uncertainties on the boundary values of the force-free parameter derived from the spectropolarimetric inversion and $|B_z|$ for the *Hinode*/SP data for 27 October. The solid line is to illustrate $\sigma \sim 1/|B_z|$ dependence and the position of the line has been chosen arbitrarily. There is a noticeable departure from the $\sigma \sim 1/|B_z|$ scaling for large values of $|B_z|$.

Table 1. Summary of magnetogram data/computational data domain sizes, field strength parameters, and relative flux balance Φ_B (see Equation (7)) for the computational models of AR 11029.

Data source	Date	$N_x \times N_y \times N_z$	$L_x \times L_y \times L_z$ (10^8 m)	$B_{\mathrm{m}} = \max(|B_z|)$ (G)	Φ_B (%)
SOLIS/VSM	Oct. 24	$236 \times 236 \times 128$	$2.0 \times 2.0 \times 1.1$	962	11
SOLIS/VSM (buffered)	Oct. 24	$270 \times 270 \times 128$	$2.2 \times 2.2 \times 1.1$	962	0.02
Hinode/SP	Oct. 27	$440 \times 300 \times 200$	$3.2 \times 2.2 \times 1.5$	2448	0.4

4. Results

This section presents the results of the force-free modeling of active region AR 11029. Section 4.1 discusses the results when the force-free code is applied to the SOLIS/VSM data for 24 October to construct P and N solutions without using the self-consistency procedure. Section 4.2 discusses the application of the self-consistency procedure to the same data. Section 4.3 discusses the application of the self-consistency procedure to the *Hinode*/SP data for 27 October.

4.1. Construction of P and N Solutions Directly from Magnetogram Data for 24 October

We construct P and N solutions for AR 11029 directly from the magnetogram data for 24 October. In this section we do not apply the self-consistency procedure. To construct the P and N solutions 50 Grad-Rubin iterations are used beginning with a potential field constructed from B_z.
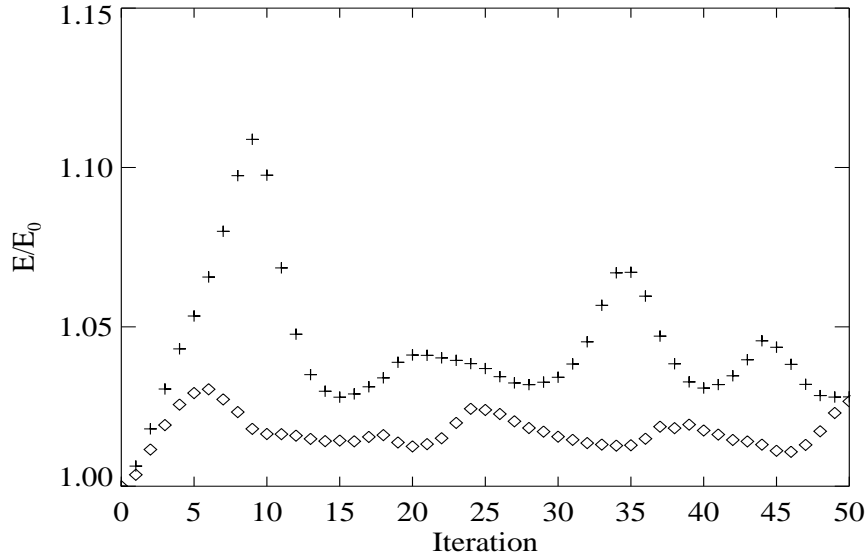
Figure 8. Results for the construction of P and N solutions directly from the SOLIS/VSM magnetogram data for 24 October. The total magnetic energy is shown (as a fraction of the energy of the potential field) for the P solution (plus signs) and the N solution (diamonds) over 50 Grad-Rubin iterations starting from a potential field. The oscillations in the energy occur because of large localized currents in the boundary data.

In application to the magnetogram data the Grad-Rubin procedure does not strictly converge for the P and N solutions. The energy of the magnetic field at each iteration provides a way to examine the convergence. Figure 8 shows the magnetic energy, E, in units of the energy of the potential field, E_0, over successive Grad-Rubin iterations for both the P and N solutions. The energy of the two solutions behaves similarly. Initially the total energy increases beyond the energy of the potential field and then begins oscillating after about 15 iterations for the P solution and after about ten iterations for the N solution. This oscillatory behavior is typical in situations where the Grad-Rubin method does not strictly converge, and may be attributed to large currents at certain points in the boundary. This is confirmed by inspecting visualizations of field lines at successive Grad-Rubin iterations. For the P and N solutions for the 24 October data we observe that the longest field lines which stretch high into the computational volume (and carry significant currents) change over successive iterations. The field in the lower part of the volume is static, and the field in the middle of the volume displays small oscillations.

We estimate the energy of the P and N solutions by averaging the energy over several Grad-Rubin iterations. After 15 Grad-Rubin iterations the P solutions stops changing systematically and begins oscillating so we estimate the energy of the P solution by taking the average energy of the field over successive Grad-Rubin iterations starting from iteration 15 [*i.e.* we take $E_P = \text{mean}(E_{15}, E_{16}, ..., E_{50})$, where E_i is the energy of the P solution after i Grad-Rubin iterations]. We do the same for the N solution, except we start the average from iteration ten [*i.e.* $E_N = \text{mean}(E_{10}, ..., E_{50})$]. We also compute the free energy $E_{\text{f}} = E - E_0$, for $E = E_P$ and $E = E_N$. The results are listed in Table 2.

The upper panel of Figure 9 shows a visualization of the magnetic field after 20 Grad-Rubin iterations (the lower panel is discussed in Section 4.2). The magnetic field

Table 2. Energy estimates for the P and N solutions constructed directly from the SOLIS/VSM magnetogram data for AR 11029 on 24 October.

Solution	E $(10^{31}$ erg $)$	E_0 $(10^{31}$ erg$)$	$E_{\mathrm{f}} = E - E_0$ $(10^{30}$ erg$)$
P	9.98	9.62	3.6
N	9.77	9.62	1.5

lines for the P solution (blue curves) and the N solution (red curves) are displayed in the upper panel. The fields are viewed looking down on the photosphere, which is colored blue where $B_z > 0$ and red where $B_z < 0$. The panel shows some qualitative difference between the P and N solutions.

The visualization of the field lines also reveals the extent to which the missing information on the boundaries influences the solution. It can be seen from the upper panel of Figure 9 that both solutions have field lines which cross the side boundaries. Many field lines connected to the trailing positive spot leave the box. However, a significant part of the active region field involves closed field lines. It is unlikely the boundary has a large influence on the final energy.

The results in this section illustrate difficulties associated with obtaining estimates for the total and free energy using the nonlinear force-free model. The Grad-Rubin iteration does not strictly converge, due to strong currents, which introduces a degree of arbitrariness in the energy estimate since the energy depends on the choice of when to stop the iteration process. Compared with the total energy the oscillations in the total energy are small, but these oscillations in the total energy translate into large oscillations in the free energy, because $E \gg E_{\mathrm{f}}$. The force-free energy estimates may be regarded as approximate (order of magnitude) estimates of the free energy. Based on the results in Table 2 we estimate that the free energy is $\approx 3 \times 10^{30}$ erg.

4.2. Construction of Self-consistent Solutions for 24 October

The self-consistency procedure is applied to the SOLIS/VSM vector magnetogram boundary data for 24 October. Initially, we use ten self-consistency cycles with 20 Grad-Rubin iterations per cycle (P and N solutions are constructed using 20 Grad-Rubin iterations, and this is repeated for ten self-consistency cycles, with the α_0-values updated using Equation (6) at the end of each cycle).

The energy of the P and N solution at each self-consistency cycle may be used to monitor the convergence of the procedure. At the end of each cycle (after 20 Grad-Rubin iterations for both P and N solutions), the total magnetic energy, E, for the solutions is calculated. Figure 10 shows the evolution of E/E_0 with cycle for the P and N solutions. Initially the two energies are different (as discussed in Section 4.1 and shown in Table 2) but after three cycles the energy approaches a single value. After ten cycles $E/E_0 = 1.0047$ for the P solution and $E/E_0 = 1.0044$ for the N solution which is lower than the energy of either the initial P or N solutions. The small difference between the energies of the P and N solutions translates into a difference of $\approx 7\%$ in the free energy. In dimensional units the free energy is about 4×10^{29} erg. The total energy of the final self-consistent solution E, the energy of the potential field E_0, and the free energy of the final self-consistent solution $E_{\mathrm{f}} = E - E_0$ are listed in Table 3 (the first two rows of this table are relevant; the second two rows are discussed below).
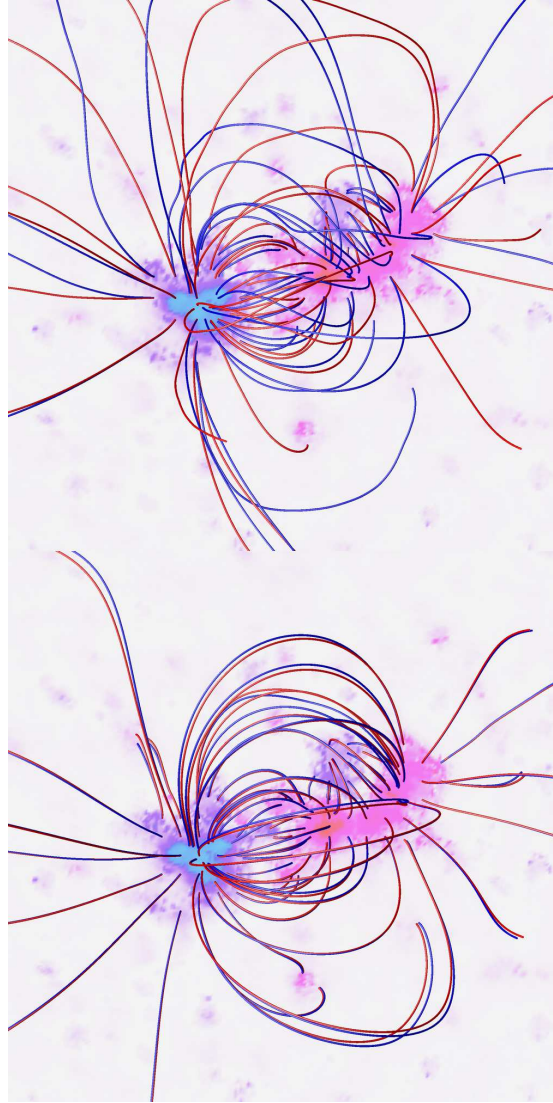
Figure 9. Nonlinear force-free models of the coronal magnetic field constructed from the SOLIS/VSM vector magnetogram data for 24 October. The P solution (blue field lines) and N solution (red field lines) are shown viewed looking down on the photosphere. The upper panel shows the two solutions constructed from the original vector magnetogram boundary data (with a flux buffer added) using 20 Grad-Rubin iterations. The lower panel shows the solutions after ten self-consistency cycles with 20 Grad-Rubin iterations per cycle. The photosphere is colored blue where $B_z > 0$ and red where $B_z < 0$. This figure illustrates the achievement of self-consistency: the P and N solutions in the upper panel are dissimilar but in the lower panel are very similar.

The lower panel of Figure 9 shows a visualization of the magnetic field of the self-consistent solutions. The magnetic field lines of the P and N solutions after ten self-consistency cycles are shown by the blue and red curves respectively. In contrast to the top panel of Figure 9, the two sets of field lines are very similar. Small differences are seen for field lines extending high into the computational volume. The agreement between the two sets of field lines confirms that a single self-consistent solution is obtained.
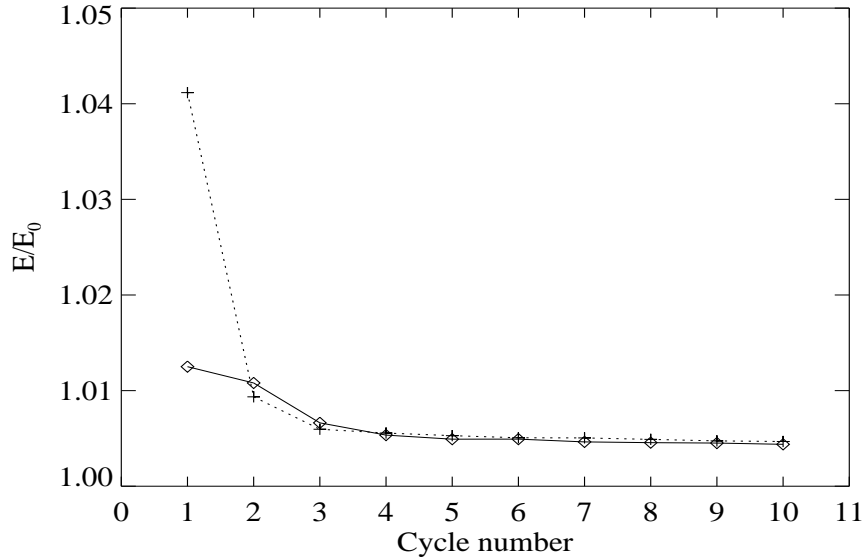
Figure 10. Results for the application of the self-consistency procedure to the SOLIS/VSM vector magnetogram data for 24 October. The energies of the P and N solutions (as a fraction of the energy of the potential field) are shown over the ten self-consistency cycles. For each cycle 20 Grad-Rubin iterations are used to construct the P and N solutions. The energy of the P solution is indicated by plus signs and a dashed line, and that of the N solution by diamonds and a solid line.

Table 3. Energy estimates for the self-consistent solutions constructed from the SOLIS/VSM magnetogram data for AR 11029 on 24 October.

Grad-Rubin iterations/cycle	Solution	E (10^{31} erg)	E_0 (10^{31} erg)	$E_f = E - E_0$ (10^{29} erg)
20	P	9.669	9.62	4.52
	N	9.667	9.62	4.23
35	P	9.666	9.62	4.20
	N	9.667	9.62	4.23

The oscillations of the energies of the initial P and N solutions (see Section 4.1) means that the magnetic field used to re-map α_0 at the end of the early self-consistency cycle depends somewhat on the number of Grad-Rubin iterations used to construct the P and N solutions. If a different number of Grad-Rubin iterations is chosen the P and N solutions have different field lines, because of the oscillations seen in Figure 8. Hence the mapping of field lines is different and the application of Equation (6) gives a different result. Correspondingly the final energy of the self-consistency procedure depends somewhat on the number of Grad-Rubin iterations used. To test this dependence we repeat the calculation with 35 Grad-Rubin iterations for the P and N solutions, instead of 20. We choose this value because it corresponds to an iteration at which the difference in energy between the P and N solutions constructed directly from the vector magnetogram data is large (see Figure 8). Once again ten self-consistency cycles are applied. The final energy and free energy in this case are also given in Table 3 in the third and fourth rows. The variation in the energies for the two self-consistent solutions with different numbers of Grad-Rubin iterations per self-consistency cycle

is sufficiently small to justify an order of magnitude (or better) estimate for the free energy of the region based on the results.

The self-consistency procedure modifies α_0 according to the procedure explained in Section 2.2. Figure 11 shows the vertical current density J_z after ten self-consistency cycles for the P solution (upper panel) and for the N solution (lower panel). The self-consistent values of J_z for the P and N solutions are very similar, confirming that a self-consistent force-free solution is found. This figure should be compared with the lower panel of Figure 3, which shows J_z for the original magnetogram data. Both Figures 3 and 11 cover the same region of the photosphere.

The currents in the lower boundary are significantly reduced as a result of the self-consistency procedure (the maximum currents are $\approx 5\,\mathrm{mAm}^{-2}$ compared with $\approx 15\,\mathrm{mAm}^{-2}$ in the original data). This is in part due to the averaging implied by Equation (6). However, it also represents the preservation of smaller but more certain values and the loss of larger but less certain values (based on the phenomenological uncertainty rule $\sigma \sim |B_z|^{-1}$). Specifically the values of α_0 are typically smaller in strong field regions, which have a smaller uncertainty, so these smaller values are better preserved in the application of Equation (6) (compared to large values of α_0 in weak field regions). There are substantial areas with $\alpha_0 = 0$ in the final self-consistent boundary data. These patches correspond to open field regions where α is set to zero by the handling of the side and top boundary conditions, as explained in Section 2.1.

4.3. Construction of Self-consistent Solutions for 27 October

The self-consistency procedure is applied to the *Hinode*/SP magnetogram data for 27 October. The initial P and N solutions again oscillate in energy. However, for the *Hinode*/SP data the oscillations are so severe that a meaningful estimate of the energy and free energy cannot be made. The large oscillations are due to large boundary values of α_0. Many of these large values have a large associated uncertainty, and hence may be spurious, but the results of the calculation are influenced by these values. It is necessary to apply the self-consistency procedure which accounts for uncertainties in α_0 and tends to remove values with large uncertainties in a systematic fashion.

The self-consistency procedure is applied to the *Hinode*/SP data for 27 October using two separate runs with a different number of Grad-Rubin iterations per cycle for each run, similar to the procedure in Section 4.2 with the SOLIS/VSM data. For the first run we use 20 Grad-Rubin iterations per self-consistency cycle, and for the second run we use 30 Grad-Rubin iterations per self-consistency cycle. We apply ten self-consistency cycles in each case. For both runs the final energies of the P and N solution converge to a single value after ten self-consistency cycles. Figure 12 shows the energy of the P solution (plus signs) and N solution (diamonds) in units of the potential field energy at the end of each self-consistency cycle over the ten cycles with 20 Grad-Rubin iterations per cycle. The results using 30 Grad-Rubin iterations are similar to those using 20 iterations per cycle. In both cases the energies of the P and N solution initially differ greatly, but after ten self-consistency cycles the energy difference is reduced to $\approx 1\%$.

The total energy, free energy of the P and N solutions, and the energy of the potential field for the self-consistency calculation are summarized in Table 4.

The total and free energy estimates differ for the two runs with different numbers of Grad-Rubin iterations, but the difference is sufficiently small to allow an order of magnitude estimate for the energy. The total energy is large (of order 10^{33} erg, which is ten times larger than was found for the region on 24 October). The variation in the free
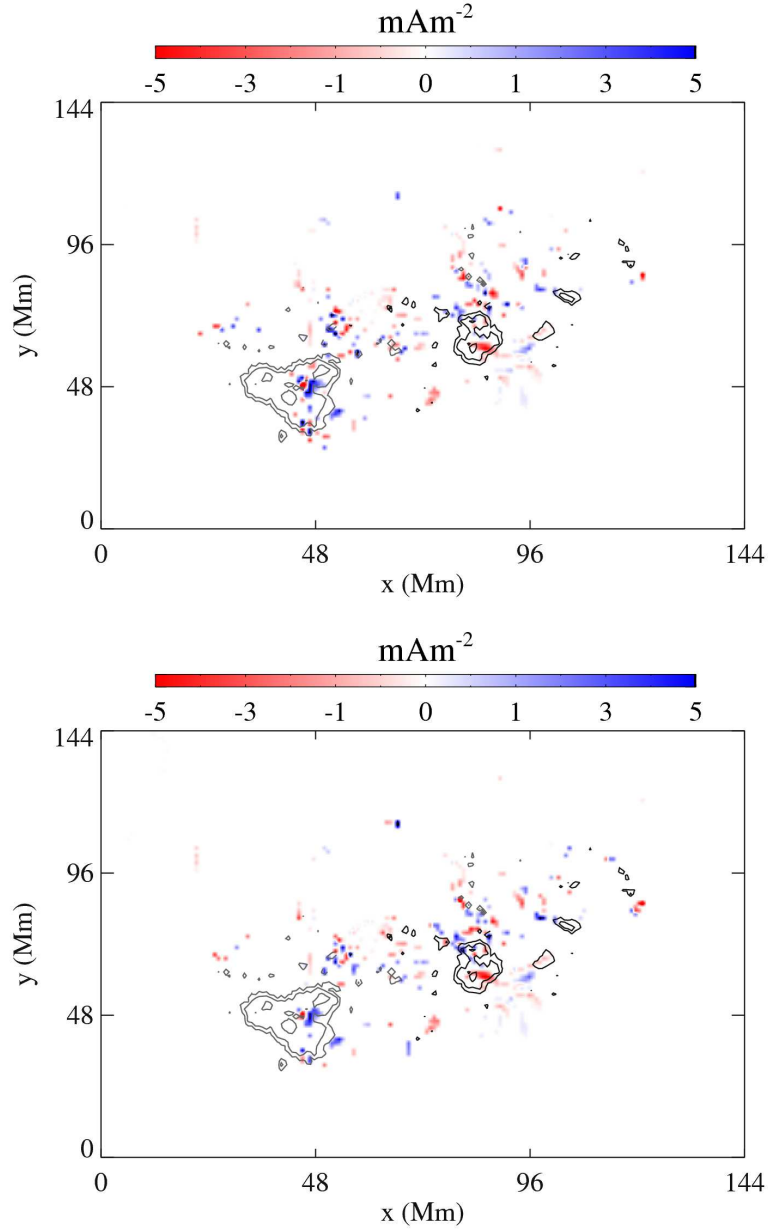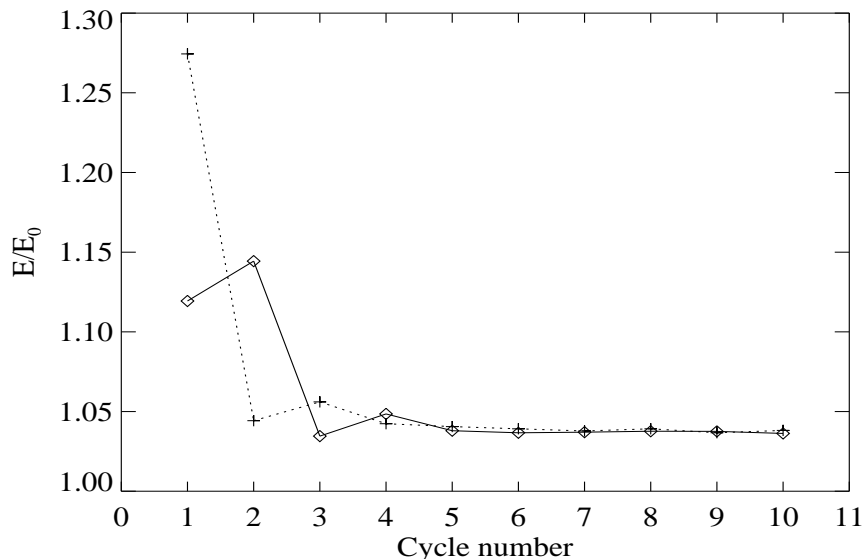
Figure 11. Results for the application of the self-consistency procedure to the SOLIS/VSM vector magnetogram data for 24 October. The vertical electric current density J_z over part of the boundary is shown for the P solution (upper panel), and for the N solution (lower panel) after ten self-consistency cycles. The values of J_z are saturated at $\pm 5\,\mathrm{mAm}^{-2}$, and only points where $|\alpha_0/\sigma|$ is three standard deviations above the mean are shown. The contours are the same as Figure 3. The distributions of J_z for the P and N solutions after the self-consistency procedure are very similar, indicating a single self-consistent solution is found.

Figure 12. Results for the application of the self-consistency procedure to the *Hinode*/SP vector magnetogram data for 27 October. The energies of the P and N solutions (as a fraction of the energy of the potential field) are shown over the ten self-consistency cycles. For each cycle 20 Grad-Rubin iterations are used to construct the P and N solutions. The energy of the P solution is indicated by plus signs and a dashed line, and that of the N solution by diamonds and a solid line.

Table 4. Energy estimates for the self-consistent solutions constructed from the *Hinode*/SP magnetogram data for AR 11029 on 27 October.

Grad-Rubin iterations/cycle	Solution	E $(10^{33}$ erg $)$	E_0 $(10^{33}$ erg$)$	$E_{\mathrm{f}} = E - E_0$ $(10^{31}$ erg$)$
20	P	1.769	1.707	6.16
	N	1.772	1.707	6.50
30	P	1.787	1.707	7.94
	N	1.791	1.707	8.35

energy is correspondingly large, but we can still place an upper bound of $\approx 10^{32}$ erg on the free energy of the active region based on the results in Table 4.

Figure 13 shows a visualization of the magnetic field of the self-consistent P solution (blue curves) and N solution (red curves) for the run using 20 Grad-Rubin iterations per cycle. The two sets of field lines are similar, although some small differences are visible.

The self-consistency procedure modifies α_0 according to the procedure explained in Section 2.2. Figure 14 shows the vertical current density J_z after ten self-consistency cycles for the P solution (upper panel) and for the N solution (lower panel). The results are shown for the run using 20 Grad-Rubin iterations per cycle, but the results using 30 Grad-Rubin iterations per cycle are similar. The self-consistent values of J_z for the P and N solutions are very similar, confirming that a self-consistent solution is found. The self-consistent values of J_z are significantly reduced by comparison with the values of J_z in the original magnetogram (lower panel of Figure 5). This is due to the averaging implicit in the procedure, and the removal by the procedure of large
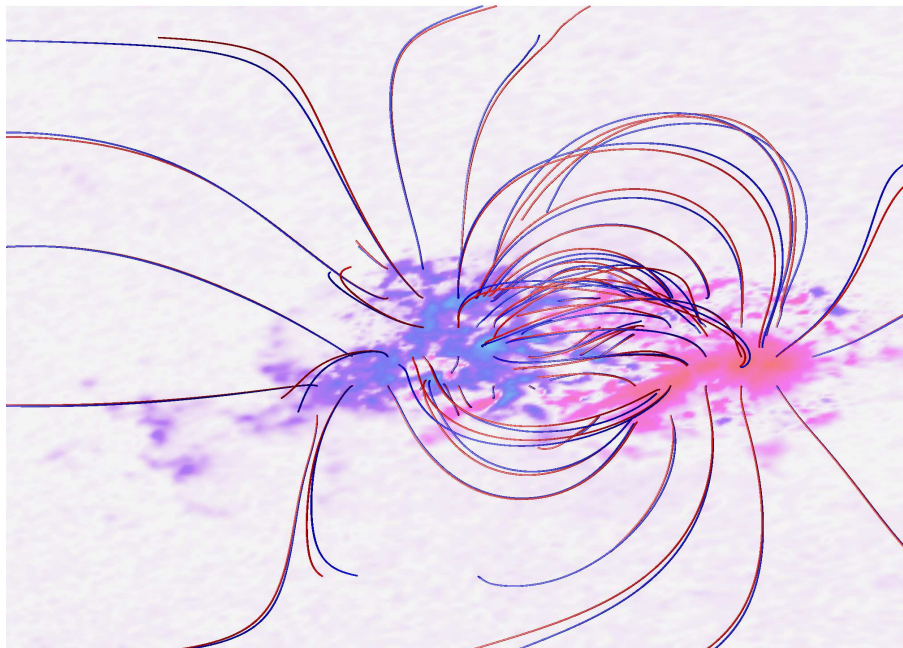
Figure 13. Nonlinear force-free models of the coronal magnetic field constructed from the *Hinode*/SP vector magnetogram data for 27 October. The self-consistent P solution (blue field lines) and N solution (red field lines) are shown for the calculation using ten self-consistency cycles with 20 Grad-Rubin iterations per cycle. The region is view looking down on the photosphere which is colored blue where $B_z > 0$ and red where $B_z < 0$.

values with large associated uncertainties (see discussion in Section 2.2). The final self-consistent boundary data contains regions with $\alpha_0 = 0$ corresponding to open field regions where α has been set to zero by the handling of the side and top boundary conditions (see Section 2.1).

5. Summary and Discussion of Results

Estimates of the total energy and free energy of the coronal magnetic field of active region AR 11029 are calculated using two vector magnetograms. The first magnetogram is based on data for 24 October from the SOLIS Vector-SpectroMagnetograph (SOLIS/VSM), and the second is based on data for 27 October obtained from the *Hinode* Solar Optical Telescope SpectroPolarimeter (*Hinode*/SP). The estimates use nonlinear force-free solutions constructed from the vector magnetogram boundary data. The magnetogram data provide two solutions to the nonlinear force-free model (the P and N solutions, denoting the choice of polarity in the boundary conditions used). The model does not have a unique solution because the boundary data are inconsistent with the model. In each case 'self-consistent' solutions (Wheatland and Régnier, 2009) are constructed taking into account uncertainties in the boundary data. For the 24 October data the uncertainties are estimated phenomenologically, and for the 27 October data the uncertainties are obtained from the inversion process used to construct the magnetogram.
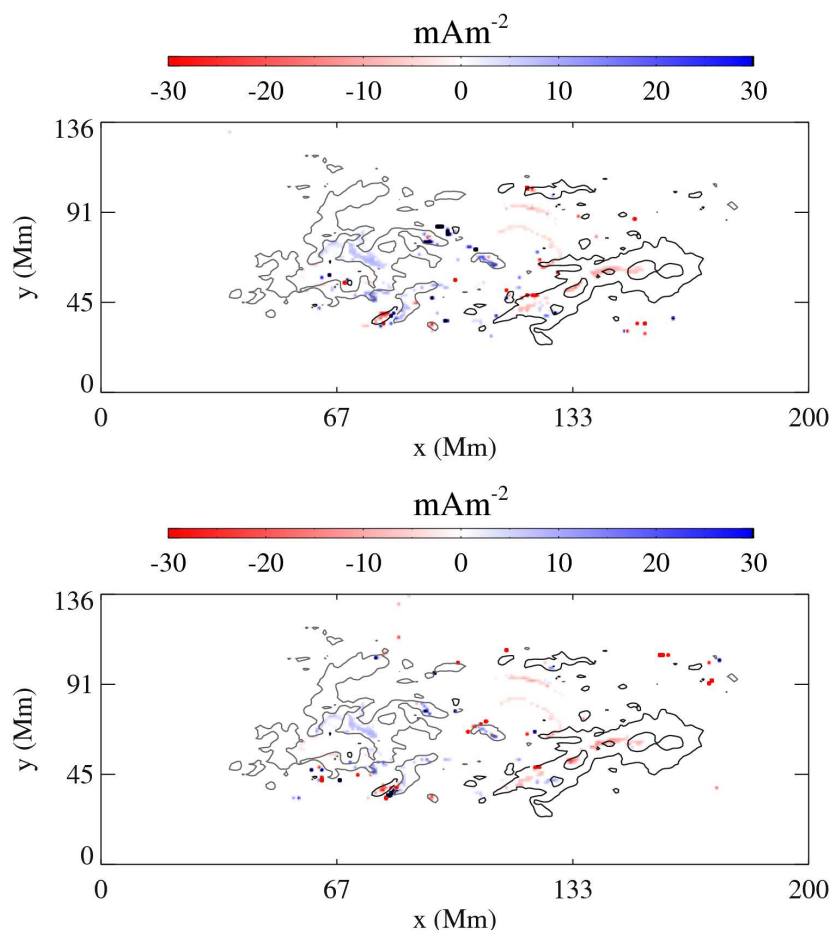
Figure 14. Results for the application of the self-consistency procedure to the *Hinode*/SP vector magnetogram data for 27 October. The vertical electric current density J_z over part of the boundary is shown for the P solution (upper panel), and for the N solution (lower panel) after ten self-consistency cycles. The values of J_z are saturated at $\pm 30\,\mathrm{mAm}^{-2}$, and only points where $|\alpha_0/\sigma|$ is three standard deviations above the mean are shown. The contours are the same as Figure 5. The distributions of J_z for the P and N solutions after the self-consistency procedure are similar, indicating a single self-consistent solution is found.

The initial P and N solutions calculated from the vector magnetogram data for 24 October have different energies and different field line structures. These solutions are themselves not uniquely defined because the Grad-Rubin iteration procedure used to construct the solutions does not strictly converge. The energy of the solutions oscillate with successive Grad-Rubin iterations owing to large currents in the boundary data. The amplitude of the oscillations in the total energy is relatively small, but the free energy is a small fraction of the total energy so this represents large amplitude oscillations in the free energy. The oscillations limit the accuracy of the estimation of the free energy, but an order of magnitude estimate is possible. The free energy of AR 11029 on 24 October is estimated from the initial P and N solutions to be $\approx 3 \times 10^{30}$ erg.

The self-consistency procedure is applied to the 24 October data. The energy of the P and N solutions agrees closely after ten self-consistency cycles, and visual inspection of the field lines of the P and N solutions confirms that a self-consistent solution is obtained. The final energy of the self-consistent solution depends only weakly on the

number of Grad-Rubin iterations per self-consistency cycle allowing a reliable estimate of the free energy. The free energy based on the self-consistent force-free solutions for 24 October is $\approx 4 \times 10^{29}$ erg. This value is roughly an order of magnitude smaller than the value obtained from the initial P and N solutions.

For the 27 October *Hinode*/SP data, the initial P and N solutions do not permit a meaningful estimate of the free energy, because of large amplitude oscillations in the energy during the Grad-Rubin procedure. The misbehavior is attributed to large currents in the boundary data, and many of these values also have large associated uncertainties. The large values prevent convergence of the Grad-Rubin iteration, and hence the result is completely determined by the spurious boundary data. We believe the self-consistency procedure which accounts for these large uncertainties provides a more reliable result. The self-consistency procedure is applied to the *Hinode*/SP data leading to the estimate that the free energy of the region is $\approx 7 \times 10^{31}$ erg on 27 October.

The results presented here illustrate the practical difficulties with force-free modeling (De Rosa *et al.*, 2009). The models constructed directly from the vector magnetogram data do not provide a unique energy estimate so we use the self-consistency procedure. The accuracy of the energy estimates obtained using the self-consistency procedure has not been tested in any independent way, and it is possible to identify aspects of the modeling which may lead to underestimation of the energy. A number of factors tend to reduce the currents in the computational volume and in turn tend to reduce the free energy. Missing boundary data on the top and sides of the computational volume is handled by setting $\alpha = 0$ along field lines which leave the top and sides of the volume. This step removes currents from the volume. The self-consistency procedure also tends to reduce the α_0 values on the lower boundary. This is due to three reasons. First, large values of α_0 which have a large uncertainty are averaged out by the weighted average in the self-consistency procedure. Second, regions with $\alpha_0 \neq 0$ connected by field lines to regions in the flux buffer with $\alpha_0 = 0$ tend to get averaged to $\alpha_0 = 0$ over successive self-consistency cycles because points in the flux buffer are assigned small uncertainties. Third, the boundary data have many small regions of α_0 with opposite sign and averaging between these regions will lead to a net decrease in α_0 over successive self-consistency cycles.

There is also considerable uncertainty associated with the boundary magnetogram data. The field values are based on inversion of spectropolarimetric measurements with finite spatial, depth, and temporal resolution, and the inversions in this case assume a Milne-Eddington atmosphere and the analytic form of the Stokes spectra described by Unno and Rachkofsky (*e.g.* Landi Degl'Innocenti and Landolfi 2004). The active region considered here, NOAA AR 11029, evolved rapidly and was highly dynamic, producing Stokes spectra which were strongly Doppler shifted and multi-lobed over much of the region. The latter indicates that the observed spectra are not consistent with a Milne-Eddington atmosphere, hence the returned field values may not be appropriate estimates of the underlying field. The inversion based uncertainties (explained in Section 3.2) for the *Hinode*/SP data reflect this somewhat but are likely underestimates. The inversions for the SOLIS/VSM data can be assumed to harbor the same concerns. There is also uncertainty associated with the resolution of the 180-degree ambiguity (Metcalf *et al.*, 2006; Leka *et al.*, 2009).

Given these caveats, it is nevertheless interesting to compare the energy of the largest flares produced by AR 11029 with the free energy estimates derived for the region, although only a fraction of the free energy is expected to be released in any single flare. To make this comparison we first establish an approximate correlation between *GOES* soft X-ray peak flux and flare energy. One measure of flare energy
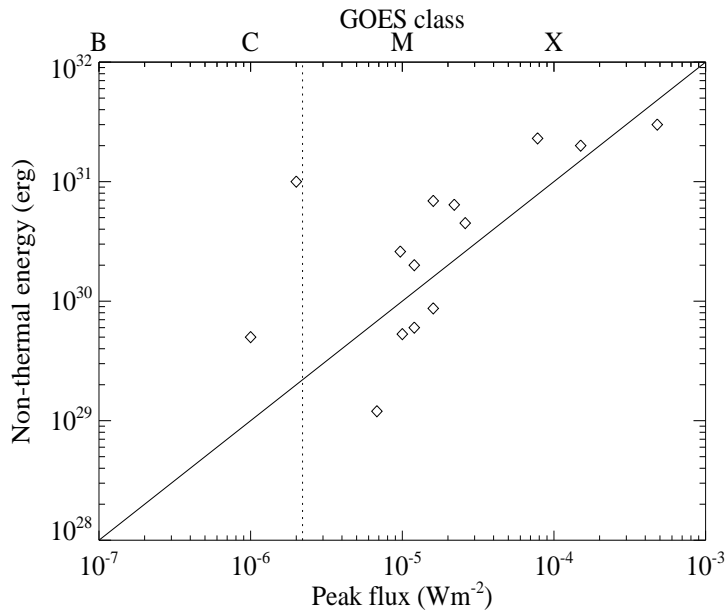
Figure 15. The relationship between RHESSI energy estimates for the non-thermal energy of a sample of flares from the literature (see Section 5) and the *GOES* peak flux of the flares. The plot also indicates the *GOES* classes. The vertical dashed line shows the peak flux of a *GOES* C2.2 class flare (peak flux of $2.2 \times 10^{-6}\,\mathrm{Wm}^{-2}$), the largest soft X-ray flare produced by AR 11029.

is the energy of non-thermal electrons, which may be inferred from hard X-ray observations (Lin and Hudson, 1971). We consider a sample from the literature of flare energies estimated from hard X-ray observations, restricting attention (for uniformity) to observations made by the Reuven Ramaty High-Energy Solar Spectroscopic Imager (RHESSI) (Lin *et al.*, 2002). These flare energies may be compared with the observed *GOES* peak flux of each event to establish an energy-peak flux scaling. Figure 15 shows the flare energy estimates made by Saint-Hilaire and Benz (2002), Saint-Hilaire and Benz (2005), Maltagliati, Falchi, and Teriaca (2006), Holman (2005) and Emslie *et al.* (2004) for 14 different RHESSI hard X-ray flares, plotted against the observed *GOES* soft X-ray peak flux of each flare. The plot shows that, to within an order of magnitude, a *GOES* B-class event has an energy of 10^{28} erg, a C-class event has energy an energy of 10^{29} erg, an M-class event has an energy of 10^{30} erg, and an X-class event has energy above 10^{31} erg. This provides a useful rule-of-thumb scaling law for flare energy estimates from *GOES* classification. These energy estimates only take into account the energy of non-thermal electrons producing hard X-rays in the flare. If an event is eruptive then a significant amount of energy can be carried off by the mass ejection (Gopalswamy et al., 2009), and active region AR 11029 produced many small eruptions during its lifetime[7].

On 24 October AR 11029 produced four B class flares, the largest of which is a B4.9 class event with a peak soft X-ray flux of $4.9 \times 10^{-7}\,\mathrm{Wm}^{-2}$. The energy of each of these flares is estimated to be of the order 10^{28} erg, which is consistent with the upper bound of 4×10^{29} erg derived from the self-consistent force-free modeling and the upper bound of 3×10^{30} erg obtained from the initial P and N solutions (Tables 2 and 3).

---

[7]See the LASCO CME catalog http://cdaw.gsfc.nasa.gov/CME_list/

On 27 October AR 11029 produced 23 soft X-ray flares. The largest flare produced by AR 11029 was a *GOES* class C2.2 which occurred at 00:24 UT on 28 October. The estimate from the modeling for the free energy is $\approx 7 \times 10^{31}$ erg (Table 4), which is comparable to an X-class flare.

Our estimates of the free energy of active region AR 11029 indicate that the region had sufficient energy to produce an M-class or X-class flare on 27 October, but not on 24 October. It is interesting that the estimate for the energy on 27 October is substantially larger than that for 24 October. The photospheric extent of the region grew rapidly during the interval 24 October to 27 October as seen in Figure 1 and Wheatland (2010), and it appears that the coronal magnetic field increased in size and energy accordingly. The magnetic flux of the region increased significantly between 24 and 27 October. On 24 October the magnetic flux was $\approx 5 \times 10^{21}$ Mx over the positive polarity and $\approx 4 \times 10^{21}$ Mx over the negative polarity. On 27 October the flux is $\approx 30 \times 10^{21}$ Mx over both polarities, an increase of a factor of 6-7.

6. Conclusion

Solar active region AR 11029 was a highly flare productive sunspot region which emerged on the Sun in late October 2009. The region produced 73 soft X-ray flares as recorded in the event list for the *Geostationary Operational Environmental Satellites* (*GOES*) over a period of about a week (24 October to 1 November). Statistical analysis of these flares showed evidence for departure from the standard power-law frequency-size distribution (Wheatland, 2010). Specifically, an absence of large events was indicated. This was conjectured to be due to the small active region having insufficient magnetic energy to power large flares (Wheatland, 2010). The aim of this paper is to test this hypothesis by estimating the free energy (*i.e.* the energy available for flaring) using nonlinear force-free modeling of the coronal magnetic field of the active region from vector magnetogram data.

Estimates of the magnetic free energy of the coronal magnetic field of AR 11029 are presented using vector magnetogram data taken by the Vector-SpectroMagnetograph at the Solar Observatory's Synoptic Long term Investigations of the Sun facility (SO-LIS/VSM), and the Solar Optical Telescope SpectroPolarimeter on the *Hinode* satellite (*Hinode*/SP). Our data set consists of a SOLIS/VSM magnetogram taken on 24 October 2009 and a *Hinode*/SP magnetogram taken on 27 October 2009. Force-free solutions are constructed from the data using the Grad-Rubin code due to Wheatland (2007) and the self-consistency procedure due to Wheatland and Régnier (2009). The procedure address the problem of the inconsistency between the force-free model and the photospheric data (Metcalf *et al.* 1995; De Rosa *et al.* 2009).

For the two vector magnetograms free energy estimates are obtained. For 24 October we estimate a free energy of $\approx 4 \times 10^{29}$ erg, which is roughly the size of a *GOES* C-class or small *GOES* M-class flare. For 27 October we estimate a free energy $\approx 7 \times 10^{31}$ erg, which is roughly the size of a *GOES* X-class flare. Although free-energy estimates made using non-linear force-free modeling are subject to significant uncertainty we believe that the order of magnitude of these estimates is correct.

The results in this paper do not support the hypothesis that there is an observable upper limit on the sizes of flares produced by small active regions due to insufficient free energy in the active region magnetic field. The modeling re-opens the interesting question of why this region did not produce any large flares given that it had sufficient energy to do so.

Appendix

Glossary of terms.

- Model: the nonlinear force-free model.
- Solution: the magnetic field $\mathbf{B} = \mathbf{B}(\mathbf{r})$ and the force-free parameter $\alpha = \alpha(\mathbf{r})$ (where $\mathbf{r}$ is the position vector) which solve Equations (3) and (4) in a domain with boundary conditions for B_z and α (over a single polarity of B_z) prescribed on the boundary of the domain.
- P Solution: a solution where boundary conditions for α are prescribed at boundary points where $B_z > 0$.
- N Solution: a solution where boundary conditions for α are prescribed at boundary points where $B_z < 0$.
- Iteration: one step in a procedure, *e.g.* one Grad-Rubin iteration is going from k to $k + 1$ in the Grad-Rubin or current-field iteration procedure, as defined in Wheatland (2007).
- Self-consistency cycle: construction of P and N Grad-Rubin solutions (involving a certain number of Grad-Rubin iterations in each case) from given B_z and α_0 boundary conditions (see Wheatland and Régnier 2009).
- Fixed point/convergence: a fixed point in the Grad-Rubin procedure is defined by $\mathbf{B}^{[k]} = \mathbf{B}^{[k+1]}$ for iterations k and $k + 1$ (see Wheatland 2007). This represents convergence of the procedure (when met for all points in a computational volume).

References

Akabane, K.: 1956, *Publ. Astron. Soc. Japan* **8**, 173.

Amari, T., Boulmezaoud, T.Z., Aly, J.J.: 2006, *Astron. Astrophys.* **446**, 691.

Aschwanden, M.J.: 2004, *Physics of the Solar Corona*, Praxis, Chichester, UK and Springer, Berlin, 196.

Bineau, M.: 1972, *Commun. Pure Appl. Math.* **28**, 77.

De Rosa, M.L., Schrijver, C.J., Barnes, G., Leka, K.D., Lites, B.W., Aschwanden, M.J., *et al.*: 2009, *Astrophys. J.* **696**, 1780.

Emslie, A.G., Kucharek, H., Dennis, B.R., Gopalswamy, N., Holman, G.D., Share, G.H., *et al.*: 2004, *J.Geophys. Res.* **109**, 10104.

Gary, G.A.: 2001, *Solar Phys.* **203**, 71.

Gary, G.A., Hagyard, M.J.: 1990, *Solar Phys.* **126**, 21.

Gopalswamy, N., Yashiro, S., Michalek, G., Stenborg, G., Vourlidas, A., Freeland, S., Howard, R.: 2009, *Earth, Moon, Planets* **104**, 295.

Grad, H., Rubin, H.: 1958, *Proc. 2nd Int. Conf. Peaceful Uses of Atomic Energy,* **31**, 190.

Georgoulis, M.K.: 2005, *Astrophys. J. Lett.* **629**, L69.

Henney, C.J., Keller, C.U., Harvey, J.W.: 2006, In: Casini, R., Lites, B.W. (eds.) *Solar Polarization 4, ASP Conf. Ser.* **358**, 92.

Holman, G.D.: 2005, *Adv. Space Res.* **35**, 1669.

Hudson, H.S.: 1991, *Solar Phys.* **133**, 357.

Hudson, H.S.: 2007, *Astrophys. J. Lett.* **663**, L45.

Hyder, C.L.: 1964, *Astrophys. J.* **140**, 817.

Jaynes, E.T., Bretthorst, G.L.: 2003, *Probability Theory*, Cambridge University Press, Cambridge, 86.

Kosugi, T., Matsuzaki, K., Sakao, T., Shimizu, T., Sone, Y., Tachikawa, S., *et al.*: 2007, *Solar Phys.* **243**, 3.

Leka, K.D., Barnes, G., Crouch, A.: 2009, In: Lites, B., Cheung, M., Magara, T., Mariska, J., Reeves, K. (eds.), *The Second Hinode Science Meeting: Beyond Discovery – Toward Understanding, ASP Conf. Ser.* **415**, 365.

Leka, K.D., Barnes, G., Crouch, A.D., Metcalf, T.R., Gary, G.A., Jing, J., Liu, Y.: 2009, *Solar Phys.* **260**, 83.

Landi Degl'Innocenti, E., Landolfi, M.: 2004, *Polarization in Spectral Lines*, Kluwer Academic Publishers, Dordrecht, 625.

Lee, J., McClymont, A.N., Mikic, Z., White, S.M., Kundu, M.R.: 1998, *Astrophys. J.* **501**, 853.

Lin, R.P., Dennis, B.R., Hurford, G.J., Smith, D.M., Zehnder, A., Harvey, P.R., *et al.*: 2002, *Solar Phys.* **210**, 3.

Lin, R.P., Hudson, H.S.: 1971, *Solar Phys.* **17**, 412.

Lin, H., Kuhn, J.R., Coulter, R.: 2004, *Astrophys. J. Lett.* **613**, L177.

Lites, B.W., Elmore, D.F., Seagraves, P., Skumanich, A.P.: 1993, *Astrophys. J.* **418**, 928.

Lites, B.W., Skumanich, A.: 1990, *Astrophys. J.* **348**, 747.

Livingston, W., Penn, M.: 2009, *EOS Trans.* **90**, 257.

Maltagliati, L., Falchi, A., Teriaca, L.: 2006, *Solar Phys.* **235**, 125.

Metcalf, T.R.: 1994, *Solar Phys.* **155**, 235.

Metcalf, T.R., Jiao, L., McClymont, A.N., Canfield, R.C., Uitenbroek, H.: 1995, *Astrophys. J.* **439**, 474.

Metcalf, T.R., Leka, K.D., Barnes, G., Lites, B.W., Georgoulis, M.K., *et al.*: 2006, *Solar Phys.* **237**, 267.

Press, W.H., Teukolsky, S.A., Vetterling,W.T., Flannery, B.P.: 1992, *Numerical Recipes in FORTRAN. The Art of Scientific Computing*, 2nd edn. Cambridge University Press, Cambridge, 124.

Priest, E.R., Forbes, T.G.: 2002,*Astron. Astrophys. Rev.* **10**, 313.

Régnier, S., Priest, E.R.: 2007, *Astrophys. J. Lett.* **669**, L53.

Sakurai, T.: 1989, *Space Sci. Rev.* **51**, 11.

Saint-Hilaire, P., Benz, A.O.: 2002, *Solar Phys.* **210**, 287.

Saint-Hilaire, P., Benz, A.O.: 2005, *Astron. Astrophys.* **435**, 743.

Scherrer, P.H., Bogart, R.S., Bush, R.I., Hoeksema, J.T., Kosovichev, A.G., Schou, J., *et al.*: 1995, *Solar Phys.* **162**, 129.

Schrijver, C.J., De Rosa, M.L., Metcalf, T.R., Liu, Y., McTiernan, J., Reǵnier, S., Valori, G., Wheatland, M.S., Wiegelmann, T.: 2006, *Solar Phys.* **235**, 161.

Skumanich, A., Lites, B.W.: 1987, *Astrophys. J.* **322**, 473.

Sturrock, P.A.: 1994, *Plasma Physics, An Introduction to the Theory of Astrophysical, Geophysical and Laboratory Plasmas*, Cambridge University Press, Cambridge, 201.

Tsuneta, S., Ichimoto, K., Katsukawa, Y., Nagata, S., Otsubo, M., Shimizu, T., *et al.*: 2008, *Solar Phys.* **249**, 167.

Thalmann, J.K., Wiegelmann, T., Raouafi, N.E.: 2008, *Astron. Astrophys.* **488**, L71.

Venkatakrishnan, P., Hagyard, M.J., Hathaway, D.H.: 1988, *Solar Phys.* **115**, 125.

Wheatland, M.S.: 2000, *Astrophys. J.* **532**, 1209.

Wheatland, M.S.: 2007, *Solar Phys.* **245**, 251.

Wheatland, M.S.: 2010, *Astrophys. J.* **710**, 1324.

Wheatland, M.S., Leka, K.D.: 2011, *Astrophys. J.* **728**, 112.

Wheatland, M.S., Régnier, S.: 2009, *Astrophys. J. Lett.* **700**, L88.

White, S.M., Kundu, M.R.: 1997, *Solar Phys.* **174**, 31.

Wiegelmann, T.: 2008, *J. Geophys. Res.* **113**, 3.